A&A 392, 239–266 (2002)
DOI: 10.1051/0004-6361:20020763

Astronomy & Astrophysics

An unbiased H_2 survey for protostellar jets in Orion A⋆

II. The infrared survey data

T. Stanke[1,2,⋆⋆], M. J. McCaughrean[2], and H. Zinnecker[2]

[1] Max-Planck-Institut für Radioastronomie Bonn, Auf dem Hügel 69, 53121 Bonn, Germany
[2] Astrophysikalisches Institut Potsdam, An der Sternwarte 16, 14482 Potsdam, Germany
e-mail: mjm & hzinnecker@aip.de

Received 14 March 2002 / Accepted 23 May 2002

Abstract. We have made an unbiased imaging survey of a 1.2 square degree area in the Orion A giant molecular cloud searching for molecular hydrogen emission line features seen in the $v = 1$–0 S(1) line at a wavelength of 2.12 μm originating in shocks in outflows from young stellar objects. This survey provides for the first time an unbiased census of outflows over a significant portion of a giant molecular cloud, and yields a sample of outflows free from selection effects and with all objects located at roughly the same, well-known distance. In this paper, we present the data gathered in the course of the survey, provide a comprehensive list of all molecular hydrogen emission features found, and give a list of the 76 candidate outflows identified in the data set.

Key words. ISM: jets and outflows – stars: formation – infrared: ISM – ISM: lines and bands – ISM: individual objects: Orion A

1. Introduction

Collimated bipolar outflows of gas are a common and perhaps ubiquitous byproduct of the star formation process (e.g., Bontemps et al. 1996b; Fukui et al. 1993; Reipurth & Bertout 1997; Richer et al. 2000). These outflows are thought to play an important role in removing excess angular momentum from accreting material, allowing the driving protostar to grow. Perhaps equally importantly, outflows impact on the surrounding molecular cloud, stirring up the material and generating turbulence. In the former case, we can learn most from detailed investigations of individual outflows, but in the latter case, we need to study whole samples of outflows in order to understand the cumulative influence of their feedback on issues such as large-scale cloud disruption.

To date, most of these samples have been drawn from a variety of star-forming regions according to certain relatively restrictive criteria. This approach carries concerns regarding selection effects and the often uncertain distance of individual sources, thus making it hard to be sure we are studying a truly typical sample of flows. A better approach would be to find a large sample of outflows in a single giant molecular cloud and thus all at a common distance, with a technique that is sensitive to a wide range of outflow properties.

The $v = 1$–0 S(1) emission line of molecular hydrogen at 2.12 μm is an important tracer of shocked gas in outflows, and is commonly associated with the jet-like structures seen emanating from young protostars (e.g., Gredel & Reipurth 1993; McCaughrean et al. 1994; Zinnecker et al. 1998; Eislöffel et al. 2000). Emission in this line is now readily imaged over large areas at high spatial resolution using sensitive large-format infrared imaging array cameras on large telescopes. Thus we have made a near-infrared imaging survey of a 1.2 square degree area of the Orion A giant molecular cloud in the 2.12 μm H_2 line, with the aim of revealing a large sample of young outflows over a significant portion of a star-forming cloud.

Initial results of this survey were presented by Stanke et al. (1998; see also 2000). In this paper, we present the full survey material in the form of large-scale images and details of all individual H_2 emission features revealed in the survey. Many of these features appear to belong to coherent jets or outflow structures, and we also present a list of these outflows along with basic information derived from the data. In subsequent papers, we will present the results of a statistical analysis of the properties of the jet and outflow sample derived from these

Send offprint requests to: T. Stanke,
e-mail: tstanke@mpifr-bonn.mpg.de

⋆ Table 2 is only available in electronic form at
http://www.edpsciences.org

⋆⋆ Visiting Astronomer, German-Spanish Astronomical Centre, Calar Alto operated by the Max-Planck-Institute for Astronomy, Heidelberg, jointly with the Spanish National Commission for Astronomy.

Table 1. List of observations made in the course of the Orion A jet survey. "np" marks observations taken under apparently nonphotometric conditions. The percentages indicate how much of the total amount of the data taken of the respective field has been taken during the respective night. The fields single 1/2/5 are single-position observations made to complete some fields (single 1 is located at the SW corner of Field 1, to the north-west of the Orion Nebula; single 2 is at the eastern edge of Field 5, roughly centered on HH 34, and single 5 is at the northern edge of Field 7, covering the L1641-C cluster).

Date	Observatory	Telescope	Instrument	What has been observed
26.12.1996	Calar Alto	3.5 m	Omega-Prime	Field 5: 2.12 μm, K'
				HH 212: 2.12 μm
11.09.1997	Calar Alto	3.5 m	Omega-Prime	Field 4: 2.12 μm, K'
				HH 211: 2.12 μm
12.09.1997	Calar Alto	3.5 m	Omega-Prime	Field 2: 2.12 μm, K' (50%)
13.09.1997	Calar Alto	3.5 m	Omega-Prime	Field 1: 2.12 μm, K' (70%)
10.01.1998	Calar Alto	3.5 m	Omega-Prime	Field 9: 2.12 μm (50%), K'
				Field 3: 2.12 μm, K'
11.01.1998	Calar Alto	3.5 m	Omega-Prime	Field 1: K' (np)
				Field 6: 2.12 μm (np)
23.10.1998	Calar Alto	3.5 m	Omega-Prime	Field 6: K' (np)
				Field 2: K'
				Field 8: 2.12 μm (np), K' (50%, np)
24.10.1998	Calar Alto	3.5 m	Omega-Prime	Field 7: 2.12 μm (np), K' (np)
				Field 8: K' (bad)
26.10.1998	Calar Alto	3.5 m	Omega-Prime	Field 7: 2.12 μm (50%, np)
				Field 9: 2.12 μm (50%), K' (50%)
				Field 8: K' (50%)
				single 5: 2.12 μm, K'
				single 2: 2.12 μm, K'
				single 1: 2.12 μm, K'
05.12.1998	Calar Alto	3.5 m	Omega-Prime	Field 7: 2.12 μm, K'(50%)
				Field 6: K' (50%)

data, and present the results of a currently ongoing effort to identify and characterise the driving sources of the jets.

2. Observations

The basic boundaries of our survey region were set by the work of Tatematsu et al. (1993), who surveyed the Orion A cloud in the CS (1–0) line using the Nobeyama 45 m millimetre telescope. They found a total of 125 dense cloud cores in their survey, and our original plan was to image all of these individually in the near-infrared, since these are possible sites where young protostars and associated outflows might be found. However, the availability of a wide-field near-infrared camera made it possible and more efficient to image the complete area covered by the CS survey, including the regions between the dense cores. This strategy also ensures a much less biased survey, with the prospect that we may ultimately be able to discuss the overall star-forming properties of the whole GMC. In addition, it became apparent as the survey was conducted that wide-field imaging was proving very useful in helping to reveal the full extent of some very long flows.

The total survey area was subdivided into nine partially overlapping fields labelled 1 to 9 (Fig. 1), with the field number increasing from north to south, or in the case of Fields 8 and 9, from west to east. The fields are typically $\sim 20' \times 27'$ in size; Field 5 is somewhat larger, covering $\sim 27' \times 33'$.

Our near-infrared survey observations were made using the wide-field camera Omega-Prime (`http://www.mpia-hd.mpg.de/IRCAM/OPRIME/`; Bizenberger et al. 1998) on the 3.5 m telescope of the Calar Alto Observatory in Spain. The camera uses a 1024×1024 pixel Rockwell International HAWAII HgCdTe array as detector with an image scale of $0\farcs396$ per pixel, yielding a field-of-view of $6\farcm7 \times 6\farcm7$. The size of the survey region and frequently bad winter weather conditions on Calar Alto meant that the survey had to be carried out over a number of observing runs, with observations made on the following dates: December 24–26 1996, September 11–14 1997, January 10–13 1998, October 23–26 1998, and December 5 1998 (see Table 1).

To identify molecular hydrogen emission line features, images were taken through a narrow-band filter (~1% bandwidth) centred at 2.125 μm, close to the wavelength of the $v = 1$–0 S(1) line of H_2. The same fields were also imaged through the broad-band K' filter (1.944–2.292 μm) in order to be able to discriminate between continuum and H_2 line emission. Typical total integration times for each field were 10 min through the narrow-band H_2 filter and 2 min through the K' filter, yielding a surface brightness sensitivity (3σ) of $\sim 10^{-19}$ W/(m^{2}arcsec^2) for extended H_2 emission line features, and a limiting magnitude of $K' \sim 17.5$ (peak pixel 3σ above the background) for continuum point sources. The emission line sensitivity is of the

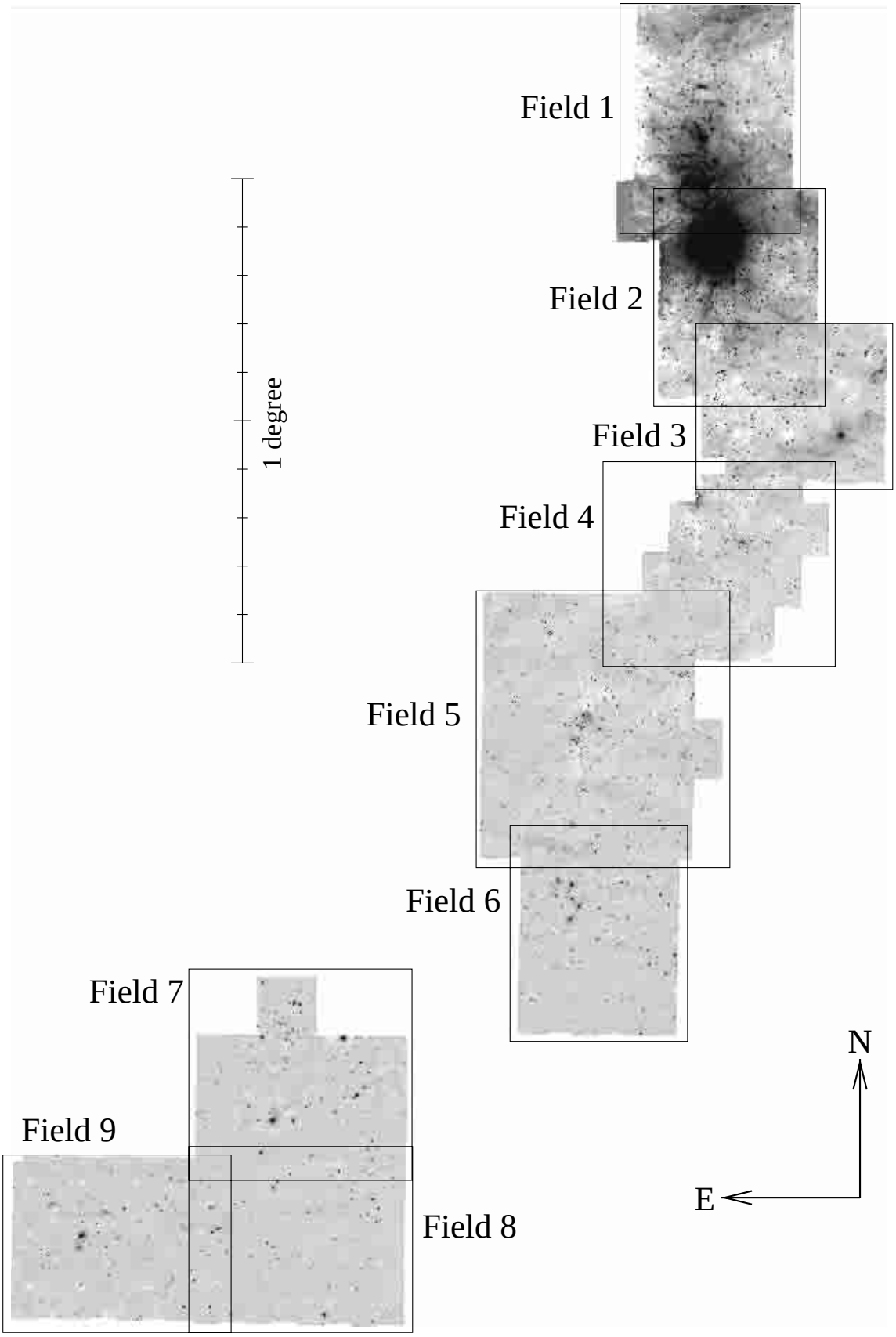

Fig. 1. Overview of the entire Orion A cloud survey area, showing a greatly reduced version of the full resolution 2.12 μm narrow band mosaic data. The boundaries of the individual survey fields are indicated by the rectangles. The size of the field is ∼2.73° in north–south direction, and ∼1.8° in east-west direction. To give a positional reference, the L1641-N IR cluster visible at the center of Field 5 is at $\alpha \sim 5^{\rm h}36^{\rm m}19^{\rm s}$, $\delta \sim -6°22'10''$ (J2000).

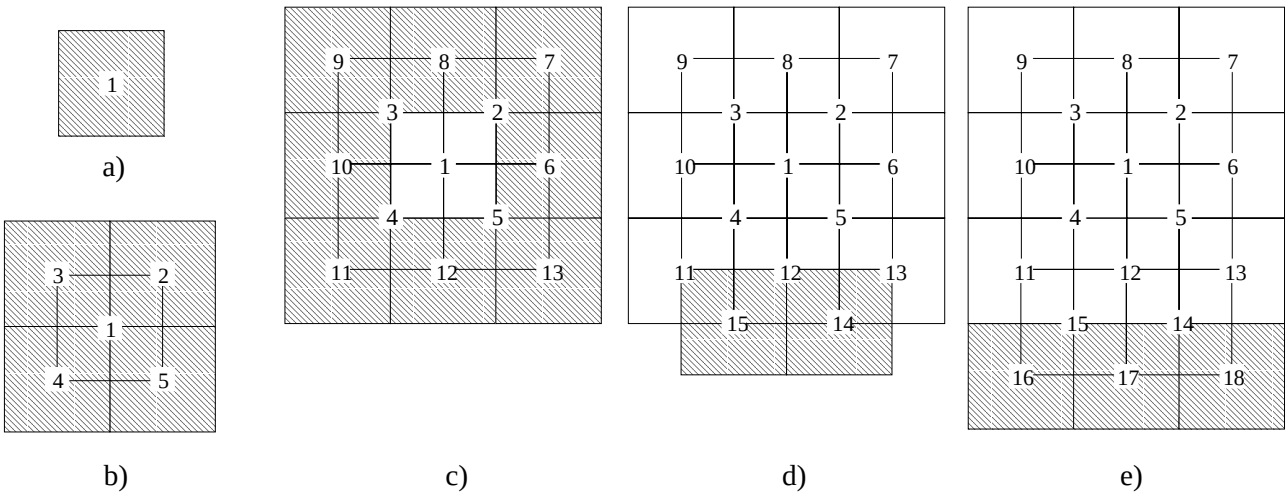

Fig. 2. Schematic representation of a typical mosaicing pattern. For each survey field, this pattern was observed once going forward, once going backward, with a small spatial offset between the forward and backward sequence.

same order as or better than that achieved in many targeted H_2 observations of individual sources found in the literature.

The detector used in Omega-Prime at that time included quite a few dead rows and columns, many adjacent to each other. Thus, a fully overlapping mosaic scheme (Fig. 2) was implemented following McCaughrean (1988), such that each position on the sky was imaged multiple times on different parts of the detector array to ensure that these bad rows and columns could be filled in with good data. Starting with an exposure at a position at the centre of a field (step a in Fig. 2), the next four exposures were taken with the array centred on the corners of the first frame (step b). Then another sequence of eight exposures was taken around this central part (step c), and so on, until the entire field was observed. The same pattern was then followed backwards, with a small shift relative to the first sequence. When combined, the inner part of such a mosaic has a uniform coverage, while the outer margin (with a width of half the camera field-of-view) has only half the integration time.

3. Data reduction

3.1. Basic reduction

The data were reduced using standard near-infrared imaging techniques. The first step was to identify bad pixels in the Omega-Prime detector array: as these increase slowly with time, this was done for each observing run. Hot pixels were identified in short exposures taken with a cold blank inserted in the filter wheel to block the external background, while cold pixels were identified in well-illuminated flat field exposures. The bad pixels were flagged in all science data frames and excluded from further processing.

A blank sky image was constructed for each science frame by median stacking a number of bracketing science frames: typically, these were the three frames immediately prior to and following the science frame in question. In regions which are relatively uncrowded and not strongly affected by large-scale extended nebulosity, this technique efficiently rejects astronomical sources and cosmic ray events, and provides a clean sky frame. A more careful selection of exposures suited for sky frame construction was necessary only in the area around and to the north of the Orion Nebula. In all cases, the resulting sky frame was then subtracted from the respective science frame. Note that this sky subtraction also removes the dark current and bias level, which have to be separately removed in optical CCD data reduction.

At the time, Omega-Prime suffered from an instability in the reset voltage of the array over the timescale of a single read-out. This effect varied from frame to frame, sometimes with smooth drifts over the time of an individual readout, other times with short spikes leading to single narrow vertical stripes in the images, and other times with rapid changes throughout the entire readout leading to a multitude of vertical stripes. These stripes were at a significant intensity level and had to be removed. To do so, a frame only containing the stripes was constructed by first replacing all data values above a certain limit (in most cases 3× the standard deviation of a frame) by the mean value of the frame, thus removing most of the stars. Then the frame was collapsed down its columns, leaving a single row containing the mean profile of the stripe pattern. A frame with the full array size was then constructed containing 1024 times this averaged profile and subtracted from the science frame, generally leading to a very good removal of the stripes. Note that this stripe removal procedure also removes any remaining offsets due to variations of the sky background.

Next, sensitivity variations of the array were corrected using flat field images. These were made nightly for each filter. Pairs of exposures were taken of the inside of the telescope dome, first diffusely illuminated by a tungsten lamp, then with the lamp off. By taking the difference between the two exposures, the cool (~280 K) background emission of the dome itself is removed, and the result should reflect the sensitivity of the detector to a ~2000–3000 K black-body spectrum, well suited to observations the sorts of cool and/or reddened astronomical objects found in star-forming regions. A number of lamp-on and lamp-off exposures were averaged, and the average lamp-off frame subtracted from the average lamp-on frame. The median intensity of the resulting difference frame was

normalised to unity. Each sky-subtracted and stripe-corrected science frame was divided by the appropriate normalised flat field image.

Finally, the individual reduced science frames had to be combined into mosaics. This was done by registering on stars in regions of overlap between frames taken at different positions. The field-of-view of Omega-Prime is large and the mosaicing pattern designed to include large overlaps, and thus there were always enough stars in the overlapping regions to do this. Some observations were made under non-photometric conditions (see Table 1), but for each survey field there was at least one sequence of observations made under good conditions. The fluxes of moderately bright stars in each field were used to determine a multiplicative correction factor to be applied to the non-photometric images. All fully reduced science frames were then combined to form a mosaic, with all data for any given point on the sky within a certain range around the median value being averaged.

3.2. Astrometric and photometric calibration

An astrometric calibration was made for the final mosaics using stars from the Hubble Space Telescope guide star catalogue[1] (GSC 1.0) which were identified on the near-infrared images. Comparison of the positions of several sources obtained with this method with positions given in the literature indicates that the positional accuracy is of the order 1″; this is about the accuracy given for the GSC (e.g., on the GSC web pages: `http://www-gsss.stsci.edu/gsc/GSC.HTML`).

The images were calibrated photometrically using stars from the UKIRT list of faint infrared standards (Casali 1992). Some subset of the stars FS 12, FS 15, FS 29, and FS 30 were observed during each run, through both the H_2 narrow-band filter and K' broad-band filters. The K' data were calibrated directly using interpolated K' magnitudes for each standard as given on the Calar Alto web pages (`http://www.mpia-hd.mpg.de/IRCAM/FAINTSTD/faintstd_kprime.html`).

The H_2 fluxes were calibrated by measuring the flux from each standard star, and then calculating the equivalent number of counts per second that would be received from a zeroth magnitude star. This was then converted into an equivalent flux density in $\mathrm{W\,m^{-2}}$ from the standard flux density value for a zeroth magnitude star in the broad-band K filter, assuming a filter bandwidth of 0.0206 μm. The result was that 1 count per second per pixel corresponds to a flux of $4.3\times10^{-20}\,\mathrm{W\,m^{-2}\,arcsec^{-2}}$. This calibration was seen to be stable to within a few percent for different nights and observing runs, and so one value was used for all the survey data. This calibration yielded fluxes for features in the L1641-N cluster in reasonable agreement (∼10–20%) with those published by Davis & Eislöffel (1995).

[1] The Guide Star Catalog was produced at the Space Telescope Science Institute under U.S. Government grant. These data are based on photographic data obtained using the Oschin Schmidt Telescope on Palomar Mountain and the UK Schmidt Telescope. The Oschin Schmidt Telescope is operated by the California Institute of Technology and Palomar Observatory. The UK Schmidt Telescope was operated by the Royal Observatory Edinburgh, with funding from the UK Science and Engineering Research Council (later the UK Particle Physics and Astronomy Research Council), until 1988 June, and thereafter by the Anglo-Australian Observatory. The blue plates of the southern Sky Atlas and its Equatorial Extension (together known as the SERC-J), as well as the Equatorial Red (ER) were all taken with the UK Schmidt.

4. Identification of individual H_2 features

Emission line objects can be identified by comparison of images taken through a narrow-band filter transmitting at the wavelength of the emission line and a suitable continuum filter. The latter can be either a narrow-band filter centred on a nearby emission-line-free wavelength or a broad-band filter. Here, the broad-band K' filter (1.944–2.292 μm) was used. This filter includes not only the 2.12 μm emission line, but several other H_2 lines in addition: in total, the detected H_2 flux in the K' filter is roughly double that through the 2.12 μm filter alone (Smith 1995). However, the broad K' filter transmits roughly ten times more continuum than the narrow H_2 filter. Thus in total, the contrast between emission-line and continuum sources is five times higher in the H_2 filter than in K', enabling them to be easily discriminated. A narrow-band continuum filter would be even more effective in separating emission-line objects particularly from nebulous continuum sources, but the broad-band K' filter was preferred in order to save telescope time: only one tenth of the H_2 integration time is needed in order to achieve the same signal-to-noise ratio for continuum features through the K' filter.

Hydrogen molecules are excited not only by shocks, but also via UV fluorescence (e.g., Black & Dalgarno 1976). H_2 line ratios can be used to discriminate between the two, but given the lack of spectral information in our survey data, we have had to rely purely on morphological information. The cooling time for shocked molecular hydrogen gas in outflows from young stars is on the order of a few years (e.g., Shull & Hollenbach 1978), and thus for a shock front moving with a velocity on the order of 100 $\mathrm{km\,s^{-1}}$, this converts to a cooling length of the order of 100 AU. This is not resolvable in our present seeing-limited observations with an angular resolution of ∼1″ corresponding to 450 AU at Orion. Thus H_2 shocks in outflows have characteristically high spatial frequencies, with bright small-scale knots and narrow filaments. UV-excited H_2 emission on the other hand arises from cloud surfaces which are exposed to strong UV radiation, and thus has a characteristically large-scale and diffuse appearance, easily distinguishable from the compact shocks.

H_2 features were identified in the reduced survey data by blinking the 2.12 μm narrow-band images against the broad-band K' images. The display values were chosen such that stars and continuum nebulosity appeared at about the same brightness in both images, and thus H_2 emission-line features appear roughly a factor of five brighter in the narrow-band image. A list of all identified H_2 features was compiled (see below), containing an identification number, the position, the H_2 2.12 μm line flux, and comments concerning the morphology of the feature. Some of the H_2 features are listed on a knot by knot basis,

while in other cases, groups of apparently related features are listed as a single entity, with more detailed astrometric and photometric information given for the individual or most prominent parts of the feature.

All feature names are prefixed with SMZ for Stanke, McCaughrean, & Zinnecker, the present authors (see Stanke et al. 1998, 2000). Then the survey field number is given, followed by a running number, usually increasing from north to south within each field. For example, the feature labeled SMZ 3-11 is feature number 11 in survey field 3. This extends the labelling introduced by Stanke et al. (1998), where only Field 5 was discussed, i.e. feature SMZ 28 in Stanke et al. (1998) is feature SMZ 5-28 in the present paper.

Figures 3 to 11 present overview images of each of the nine survey fields, with all H_2 features or groups of features marked and labelled. Table 2 then shows a set of detailed images showing the respective feature from the H_2 2.12 μm narrow-band image, the broad-band K' image, and a continuum-subtracted image. For each feature, a 20″ scale-bar is shown. Column (a) then gives the SMZ identification number; Col. (b) gives the coordinate of the features (J2000) and/or the positions of some prominent parts of the respective feature; Col. (c) gives the 2.12 μm line flux in 10^{-17} W m^{-2}. Also given is the number of the H_2 jet which the feature is believed to belong to (see Sect. 5). Jets listed in bold-face (e.g., **#3**) are for those where the jet identification is thought to be fairly certain; those marked in normal face (e.g., # 1) are less certain. Finally, Col. (d) gives a comment on the morphology, the associated optical Herbig-Haro object number (if applicable), and for Field 1, the YBD number given by Yu et al. (1997) to features related to the OMC-2/3 outflow system.

5. The H_2 flows

The main aim of our survey was to locate jets and outflows, and it is clear that many of the H_2 emission-line knots and filaments found in the survey as presented in Table 2 appear to be parts of larger structures. In this section, we attempt to define a sample of jets and outflows. However, it must be recognised at the outset that this is not a wholly objective process, given the wide variety in possible flow lengths and morphologies. As far as possible, we have followed some basic rules in order to exclude too many spurious identifications. For example, for obvious reasons, we have chosen not to regard isolated pairs of knots as flows, although of course it is possible that in some cases they may form one. Overall however, we have had to address the identification of flows on a case by case basis in a qualitative fashion, and in order to reflect this, the flows were divided into two groups:

- **The "certain" group:** this group includes flows whose identifications are regarded as quite secure based on morphological grounds. The names of flows in this group are printed in bold face;
- **The "uncertain" group:** this group includes flows whose identifications are insecure as only poorly constraining H_2 features were found, and flows which are known to be real, but which are not necessarily recognisable based on our H_2 data alone. An example of the latter group is the flow from the T Tauri star Haro 4-255 (flow # 73), which is a well-collimated optical Herbig-Haro jet terminating in a bow shock (Aspin & Reipurth 2000). In H_2, only a faint wisp of the bow shock is visible, from which alone it would be impossible to identify the flow. The names of flows in this group are printed in plain face.

With these constraints in mind, it is possible that some of the flows identified in our survey, particularly those from the uncertain group, may subsequently turn out not to form a flow as suggested here, with their H_2 knots belonging to other systems. These and other caveats are explored in more detail below.

Table 3 lists the candidate protostellar H_2 jets and outflows that we have identified, along with basic information for each. Column 1 gives the name of each flow; flows regarded as certain are listed in bold face; uncertain flows are listed in plain face. Columns 2 and 3 give a representative coordinate for the jet, as follows. If there is a candidate driving source, its position is given; alternatively, if the location of a possible driving source is suggested on morphological grounds, e.g., the geometric centre of a apparently bipolar H_2 configuration, this position is given. Failing this, the position of a prominent part of the candidate H_2 flow is given. Column 4 gives a list of H_2 features thought to be associated with the respective flow. Columns 5 and 6 give the projected length of the flow in arcminutes and in parsecs, respectively, the latter assuming a distance to the Orion A cloud of 450 pc. Column 7 gives the position angle of the flow (degrees east of north). Column 8 gives the luminosity $L_{2.12}$ in the $v = 1$–0 S(1) line in $10^{-4}\,L_\odot$ (of all H_2 features associated with the flow; no corrections for the unknown extinctions were applied). The total H_2 luminosity L_{H_2}, which accounts for emission in other H_2 lines, may be roughly calculated by multiplying $L_{2.12}$ by 10. Column 9 lists any association between the H_2 flows and the CS cores of Tatematsu et al. (1993). This field is left blank if the flow lies outside the CS survey area or too close to its edge; a dash marks flows apparently not associated with a CS core; and the flag ON (**#26**, **#27**, and **#28**) marks those flows which are not included in the analysis to be presented in subsequent papers because they lie too close to the Orion Nebula. Finally, we also give the H_2 luminosity and length of two prototype H_2 jets, HH 212 and HH 211, since they are used frequently for comparison throughout this work.

Furthermore, an overview of each field is shown. Candidate outflows regarded as rather certain are marked by solid lines and bold letters, while flows regarded as uncertain are marked with dashed lines and plain letters (Figs. 12 to 20). On these maps, the H_2 features as listed in Table 2 are also marked as in the overview maps in Figs. 3 to 11 with grey symbols.

5.1. Results in summary

A total of 76 candidate flows have been identified. The bright nebulosity of the Orion Nebula means that only the brightest flows can be seen in that area, which introduces a bias towards brighter flows. Thus, flows found in the Orion Nebula area (flows **#26**, **#27**, and **#28**) are not included in the statistical

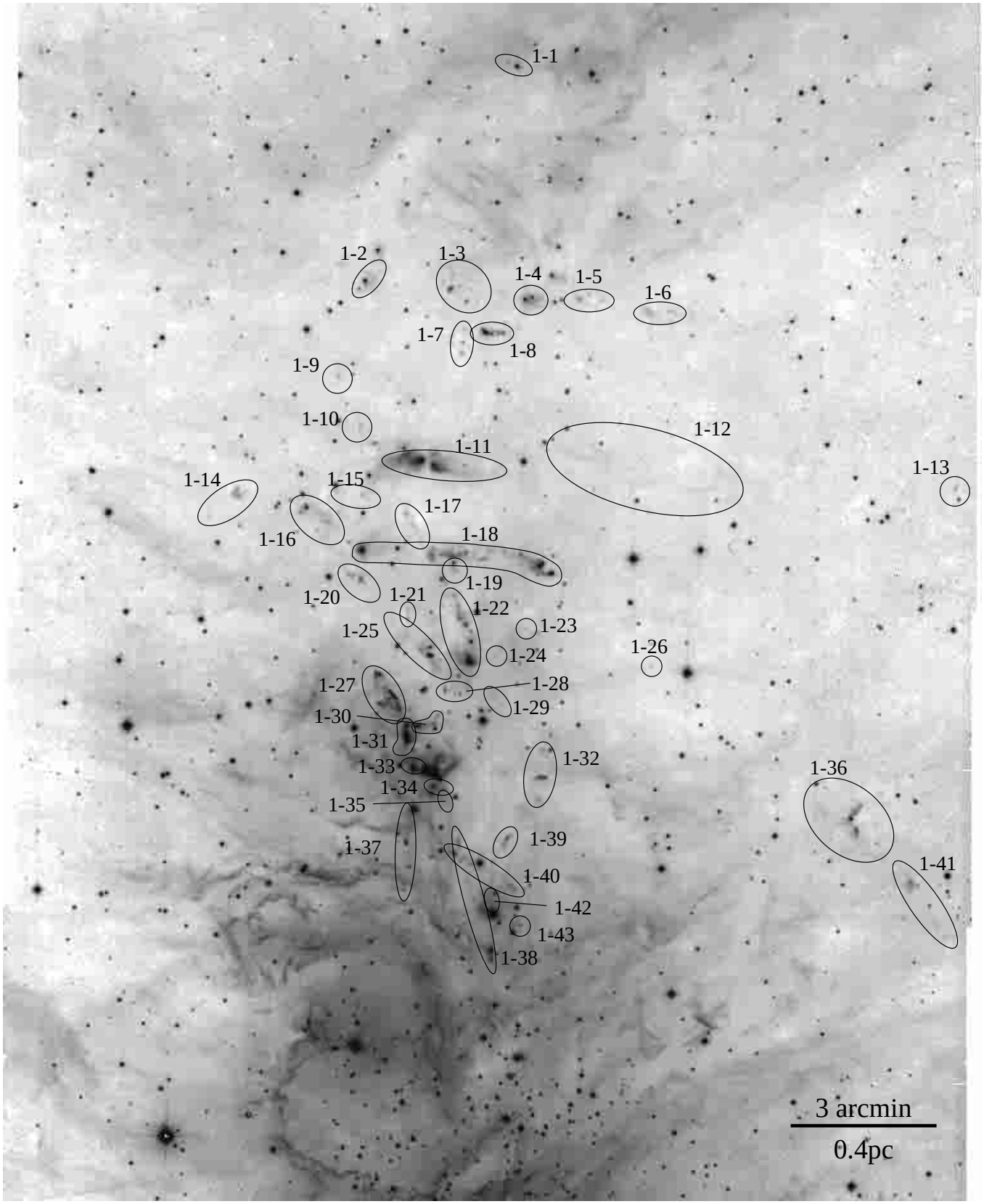

Fig. 3. H_2 features in Field 1 (the OMC-2/3 area). The figure shows the 2.12 μm narrow band image (not continuum subtracted) in logarithmic intensity scaling. The size of the field is $20\farcm3 \times 25\farcm1$, centered on $\alpha = 5^h35^m20\fs6$, $\delta = -5°06'20''$ (J2000). North is up, east to the left.

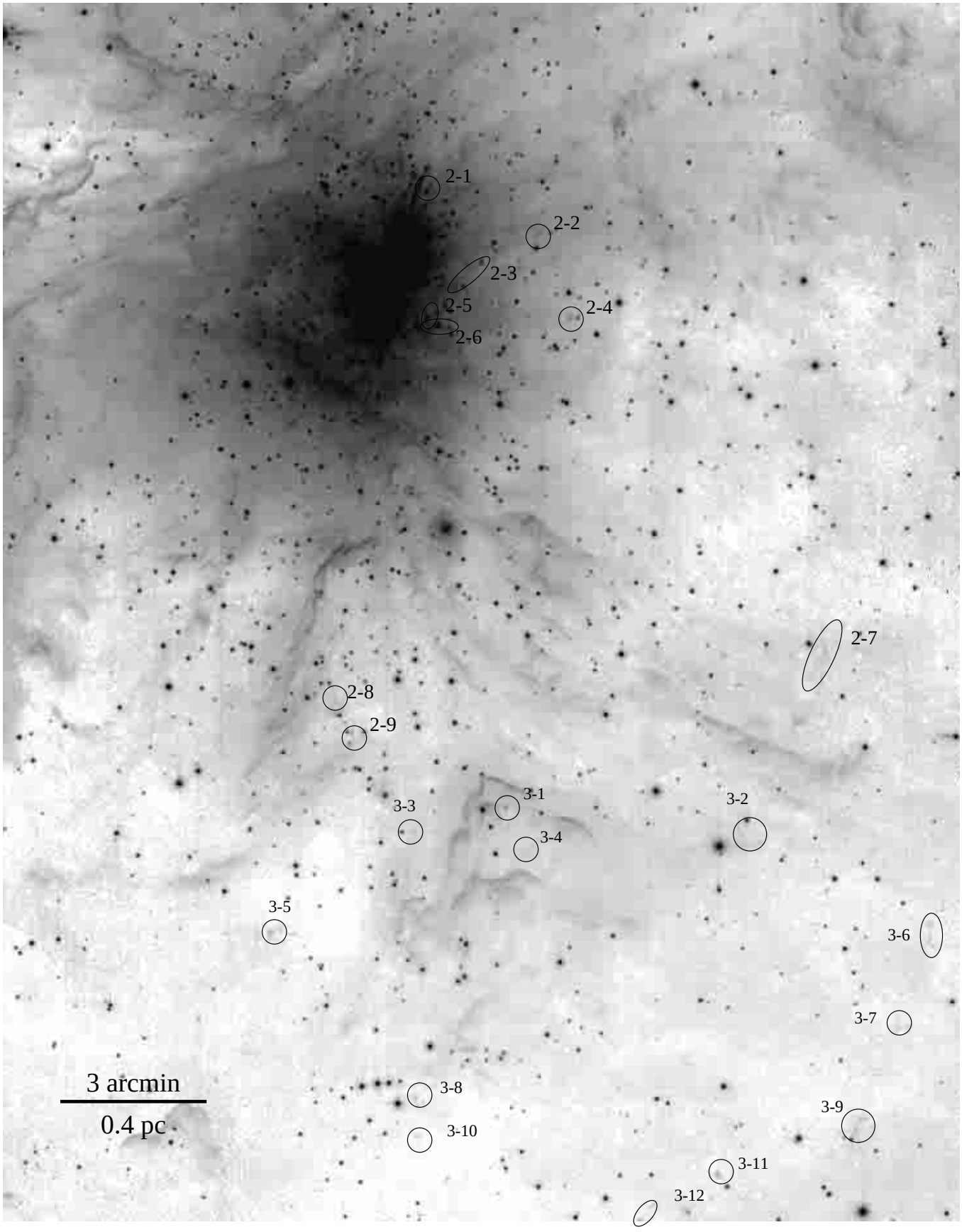

Fig. 4. H_2 features in Field 2 (the Orion Nebula area). The figure shows the 2.12 μm narrow band image (not continuum subtracted) in logarithmic intensity scaling. The size of the field is $19\farcm8 \times 24\farcm7$, centered on $\alpha = 5^h35^m07\fs5$, $\delta = -5°29'34''$ (J2000). North is up, east to the left.

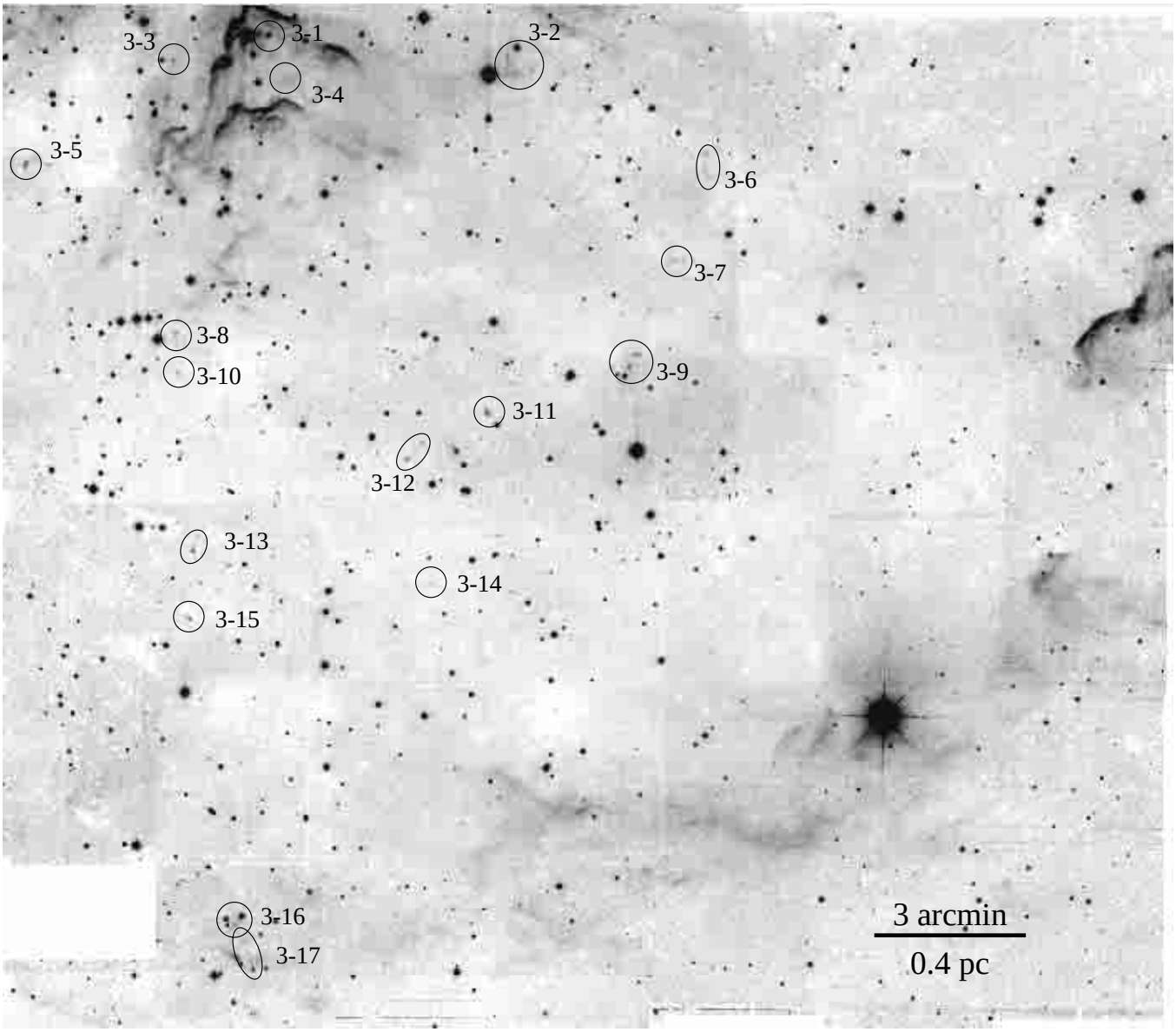

Fig. 5. H_2 features in Field 3 (the area south of the Orion Nebula). The figure shows the 2.12 μm narrow band image (not continuum subtracted) in linear intensity scaling. The size of the field is $23\farcm2 \times 20\farcm3$, centered on $\alpha = 5^h34^m38\fs3$, $\delta = -5°42'56''$ (J2000). North is up, east to the left.

analysis in the subsequent papers, except where noted. We are then left with 73 flows, of which 44 (60%) belong to the certain group and 29 (40%) belong to the uncertain group. Note that the Orion Nebula flows would belong to the certain group.

5.2. Notes on individual flows

In the following, short notes are given for each individual flow. In many cases, this note also mentions the suspected driving source, as identified in either published data or publicly available data (e.g., IRAS data), or as seen in our own data. However, the identification of the driving sources and their further characterisation remains incomplete, and a more detailed and complete discussion of the jet driving sources is deferred to a future paper.

The acronym CRW denotes the millimetre continuum sources found in OMC-2/3 by Chini et al. (1997), while "RN" stands for "reflection nebulosity".

1: Two knots east and west of IR star (candidate source). Position refers to this star.
2: Two knots & some more diffuse emission; associated with IR–RN and star. Position refers to H_2 knot SMZ 1-2 A.
3: Chain of compact knots and filamentary structures. Position refers to the candidate driving source IRS 1.
4: North-south chain of compact knots. Position refers to the candidate driving source CRW MMS6.
5: East-west chain of bright compact knots; well-collimated jet. Position refers to the candidate driving source CRW MMS5.
6: East-west system of compact knots (close to bipolar Haro 5a/6a RN); weak filamentary structures further west;

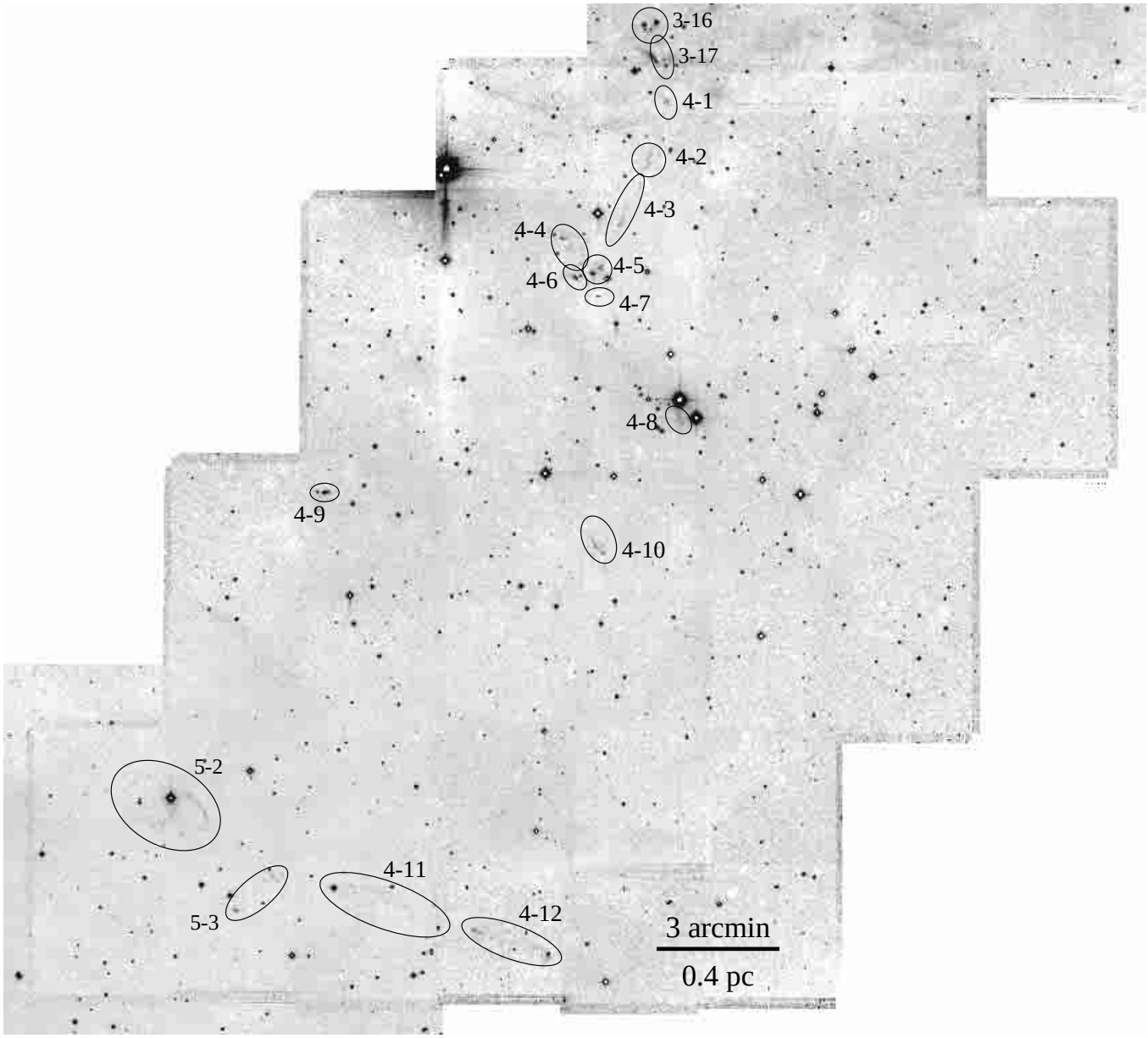

Fig. 6. H_2 features in Field 4. The figure shows the 2.12 μm narrow band image (not continuum subtracted) in linear intensity scaling. The size of the field is 27.′8×25.′1, centered on $\alpha = 5^h35^m12.^s8$, $\delta = -6°03'07''$ (J2000). North is up, east to the left.

in addition to the H_2 features noted here, HH 41, HH 42, HH 128, and HH 129 (11′ to the east) are presumably also part of this flow (see Reipurth et al. 1997). Measured over the H_2 features only (including the HH objects east of Haro 5a/6a, the flow would extend over a total of about 24′ or 3.1 pc). Position refers to the candidate driving source CRW MMS7 (Haro 5a/6a).

7: Long, narrow chain of compact features; apparently well-collimated flow; H_2 features SMZ 1-22 and SMZ 1-24 may form an independent flow (#13). Position refers to the candidate driving source (U-shaped continuum nebula associated with SMZ 1-17 A).

8: 1-15: chain of compact knots; the extension of a line through these knots leads through SMZ 1-14; very uncertain. Position refers to SMZ 1-15 A.

9: Broad, well-defined, collimated, bright flow. Position refers to candidate driving source CRW MMS9.

10: Possible flow from CRW MMS10 or bright IR source nearby SMZ 1-18 H; very uncertain. Position refers to bright IR source near SMZ 1-18 H.

11: Very uncertain: SMZ 1-19 is presumably a bow shock in a flow running south-north; parts of SMZ 1-22 possibly belong to this flow. Position refers to SMZ 1-19 B. Length and H_2 luminosity are measured over SMZ 1-19 only.

12: 2 knots, marking possible north-south oriented flow; knots are elongated along suspected flow direction; well collimated (?). Position refers to middle of gap between the two knots.

13: Possible well-collimated flow from CRW FIR1c. Position refers to suspected K' counterpart to FIR1c.

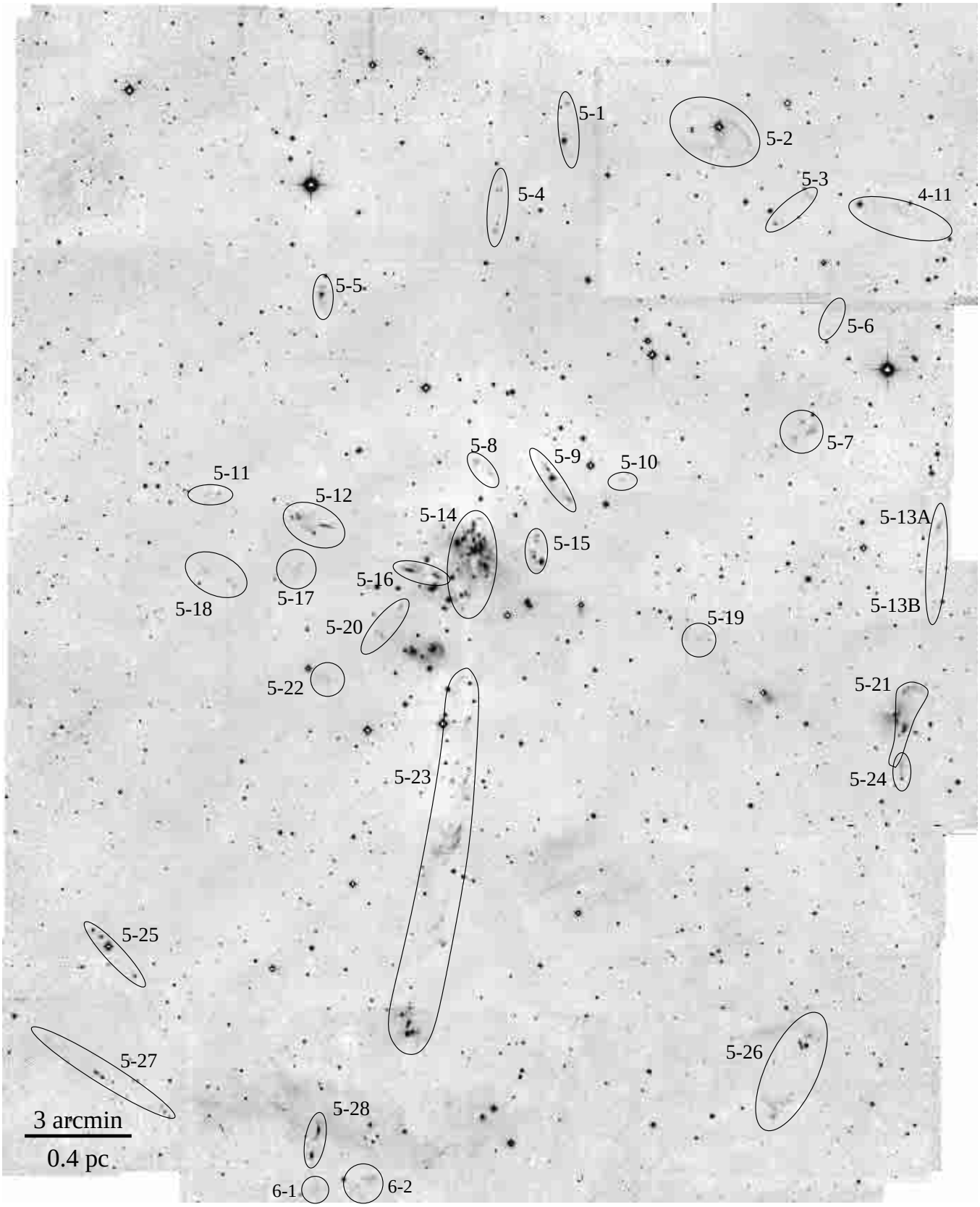

Fig. 7. H_2 features in Field 5 (the area around the L1641-N cluster, see also Stanke et al. 1998). The figure shows the 2.12 μm narrow band image (not continuum subtracted) in linear intensity scaling. The size of the field is $27\farcm6 \times 33\farcm8$, centered on $\alpha = 5^{\rm h}36^{\rm m}17\fs2$, $\delta = -6°23'31''$ (J2000). North is up, east to the left.

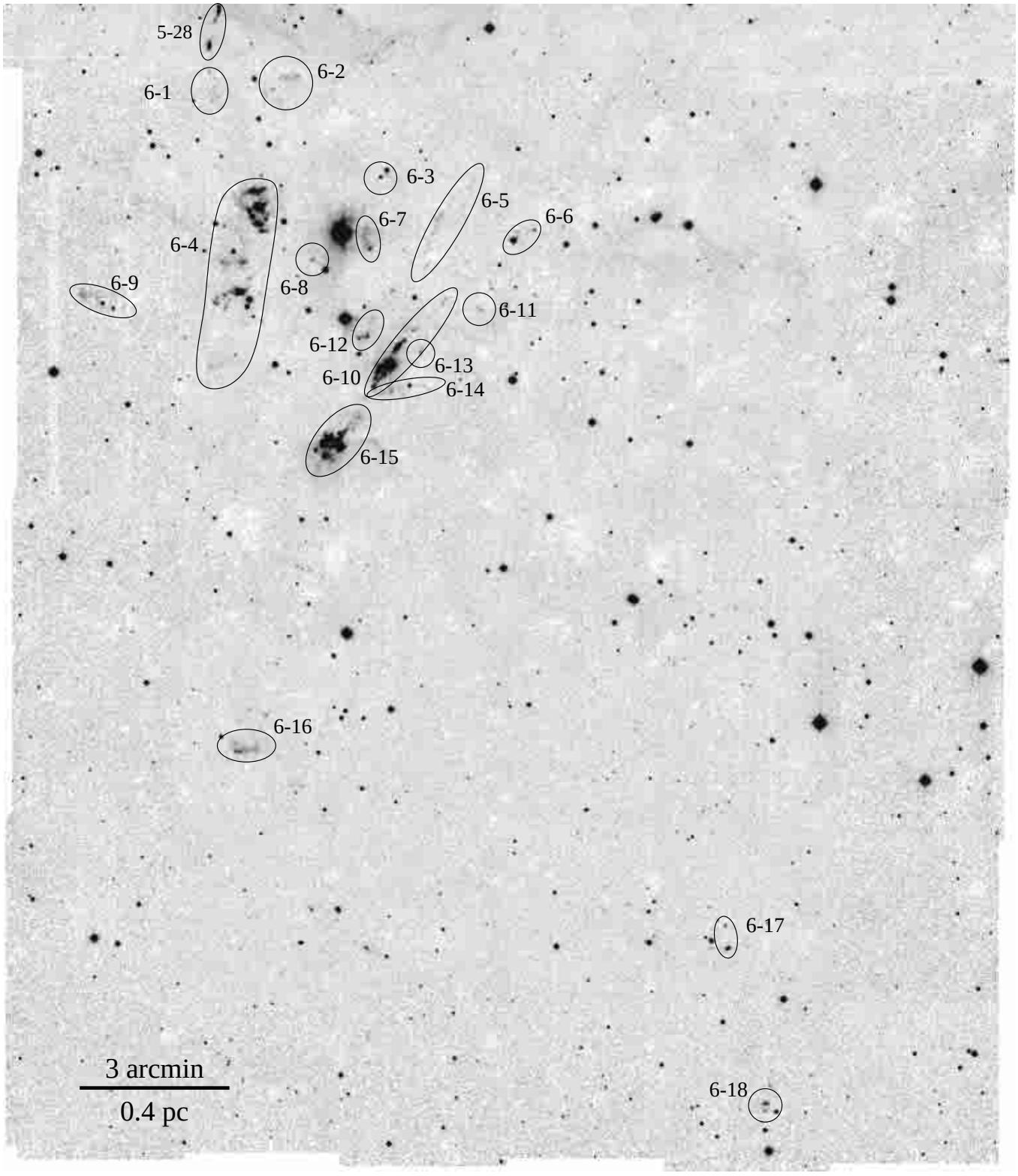

Fig. 8. H_2 features in Field 6 (the HH 1/2 and V 380 Ori area). The figure shows the 2.12 μm narrow band image (not continuum subtracted) in linear intensity scaling. The size of the field is $20\farcm3 \times 23\farcm5$, centered on $\alpha = 5^h36^m11\fs2$, $\delta = -6^\circ\ 50'02''$ (J2000). North is up, east to the left.

14: Long chain of H_2 knots and partially optically visible HH-objects; well collimated; the full extent of the flow is not clear. Length is measured over SMZ 1-20 to SMZ 1-28; adding SMZ 1-16 and SMZ 1-32, the flow extends over 1 pc. Position refers to the suspected driving source.

15: SMZ 1-22 F and some additional knots comprise possible flow from bright NIR source south-west of SMZ 1-22 F or FIR1b; very uncertain. Position refers to FIR1b. Length and position angle are measured from the bright IR source out to the H_2 features.

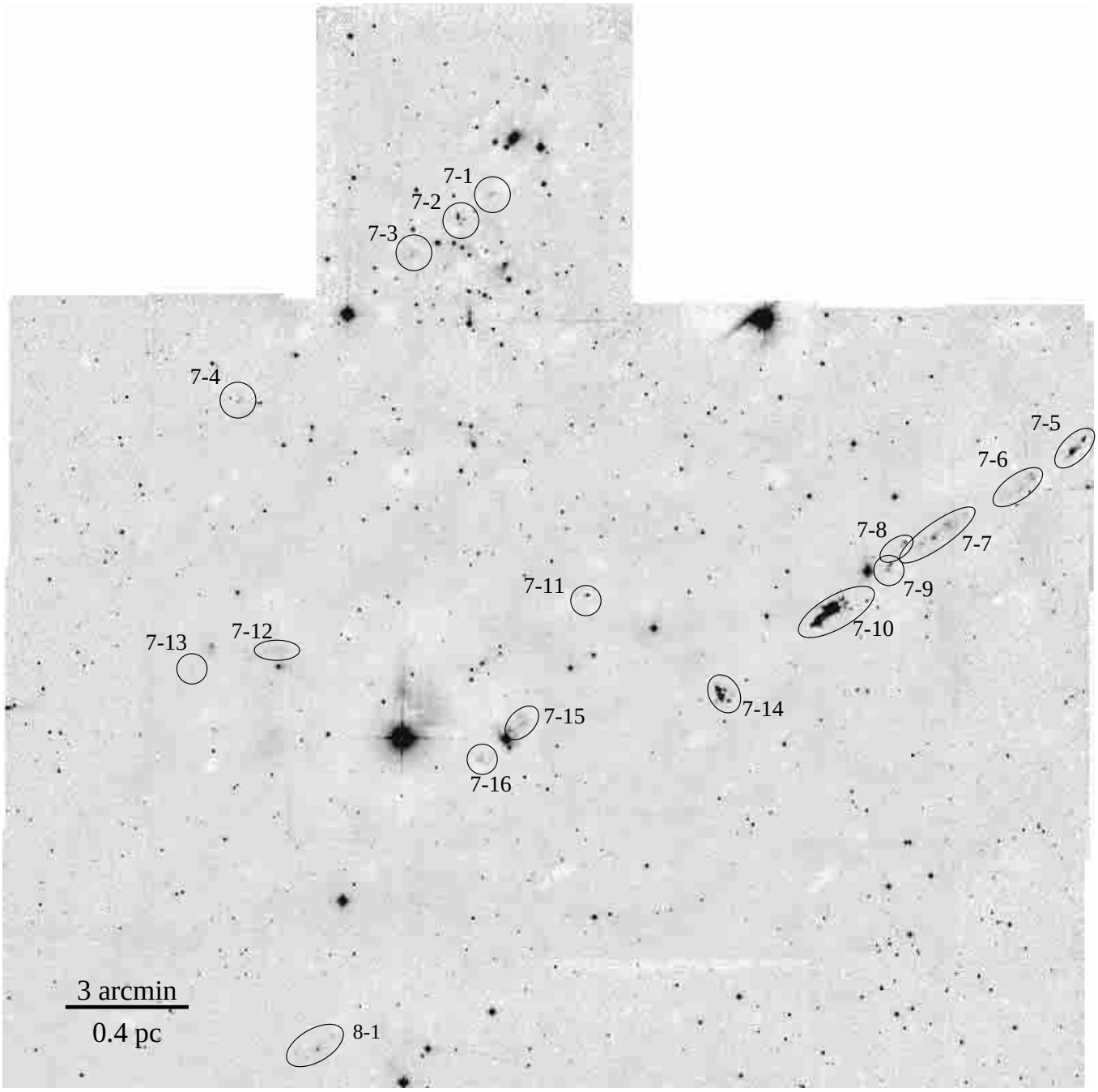

Fig. 9. H_2 features in Field 7 (the L1641-C and HH 43 area). The figure shows the 2.12 μm narrow band image (not continuum subtracted) in linear intensity scaling. The size of the field is 26.′7 × 27.′5, centered on $\alpha = 5^h38^m39.^s0$, $\delta = -7°08'35''$ (J2000). North is up, east to the left.

16: SMZ 1-28: chain of compact knots: jet? SMZ 1-29: possibly part of a bow shock; very uncertain. Position refers to candidate driving source CRW FIR2.

17: SMZ 1-27 A, C, D: Spindle-shaped outflow lobe running from south-west to north-east; SMZ 1-27 A bow shock; SMZ 1-34 lies symmetrically with respect to SMZ 1-27 A about the candidate outflow source. Position refers to candidate driving source, a K'-counterpart to CRW FIR3.

18: This flow is superimposed on **#17**; spindle-shaped outflow lobe, similar to **#17**, but smaller; counterlobe not seen. Position refers to candidate driving source.

19: Short, well-collimated H_2 and optical jet flowing through narrow, illuminated cavity. Position refers to the candidate driving source at the base of the cavity.

20: All knots are located roughly along a line, but this flow identification is regarded as very uncertain. Position refers to the candidate driving source (also very uncertain).

21: North-south running chain of compact features, presumably originating somewhere in the FIR3/4/5 complex, but no driving source identified. Knots SMZ 1-37 B and C may form independent flow (see #22). Position refers to northernmost H_2 feature (SMZ 1-37 E).

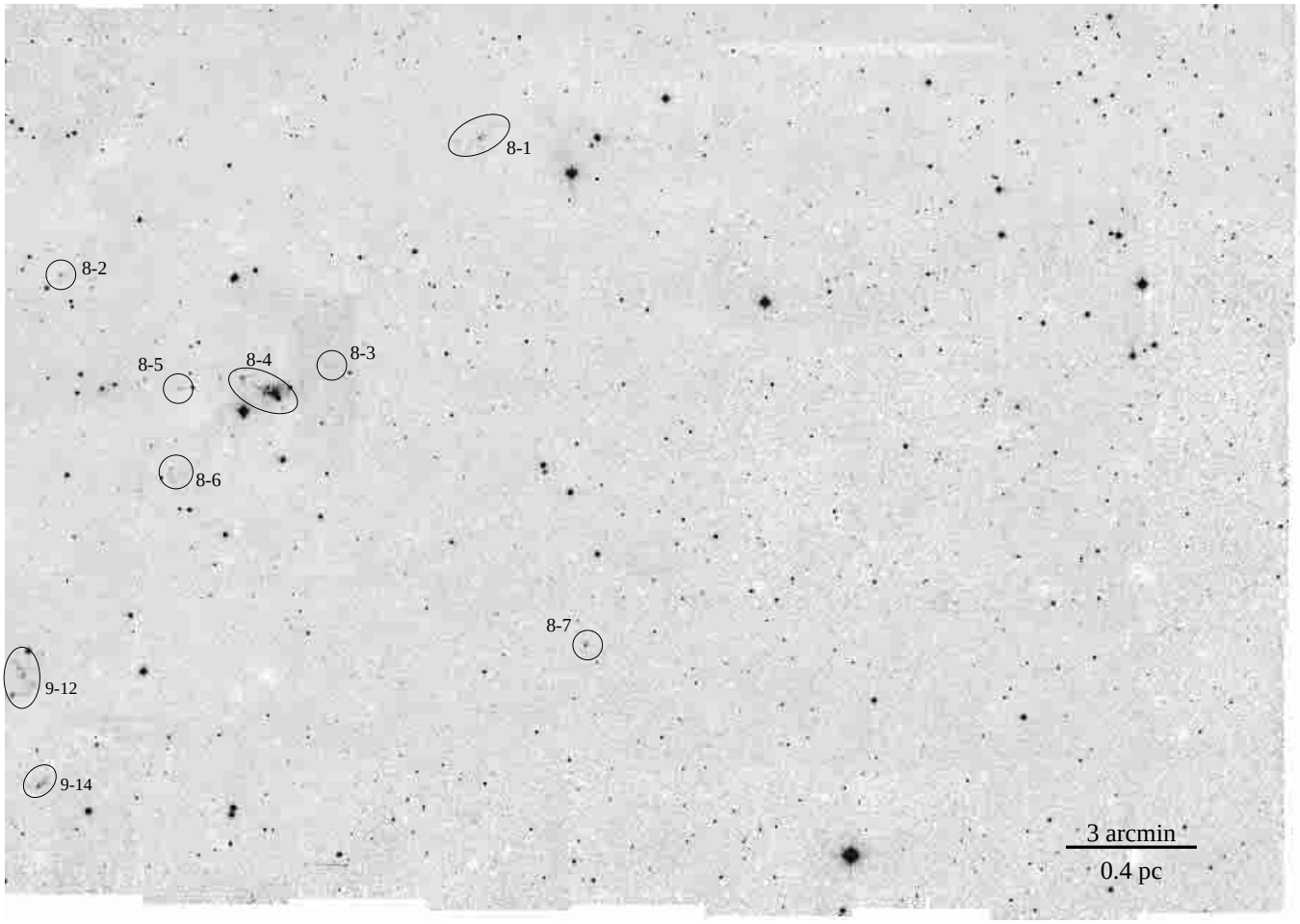

Fig. 10. H_2 features in Field 8. The figure shows the 2.12 μm narrow band image (not continuum subtracted) in linear intensity scaling. The size of the field is $29\farcm3 \times 21\farcm1$, centered on $\alpha = 5^h38^m44\fs0$, $\delta = -7°27'43''$ (J2000). North is up, east to the left.

22: SMZ 1-37 B and C may form a spindle-shaped flow independent of **#21**; no driving source identified. Position refers to point between SMZ 1-37 B and C.

23: Chain of compact knots (SMZ 1-35 A,B; SMZ 1-37 E, D, C, B) on line running through SMZ 1-37 A (bow shock?), suggesting a well-collimated jet beam. Position refers to the candidate driving source.

24: Spindle-shaped, partly limb-brightened outflow lobe. Driving source is close to SMZ 1-40 A; SMZ 1-40 B appears to be leading working surface; no visible counterflow. Position is candidate driving source.

25: Poorly-defined, apparently poorly-collimated flow. Position refers to the candidate driving source CRW FIR6c; however, the source identification is uncertain.

26: Chain of knots, presumably collimated jet. SMZ 2-3 A appears to be a bow shock in the flow. Position refers to the candidate driving source.

27: Short, highly-collimated jet beam embedded in a spindle-shaped cocoon. Position refers to the southern end of the jet, presumably close to the driving source, which itself is not identified. No counterflow detected. The association of knot SMZ 2-5 C with this flow is unclear.

28: East-west chain of H_2 features. Length is measured over SMZ 2-6 only; total length measured over SMZ 2-5 C, SMZ 2-6, and SMZ 2-4, is about $3'$ or 0.4 pc. Flow is apparently well-collimated. Position refers to SMZ 2-6 A (no source identified).

29: System of faint H_2 features distributed in bipolar manner around the driving source. SMZ 3-2 appears to be a large bow shock. Position refers to the driving source.

30: Two knots, north and south of a red nebulous star, very uncertain. Position refers to the red star.

31: Poorly-defined chain of features, possibly delineating flow from K' continuum source close to SMZ 3-9 A; alternatively, there may be a flow running from north-west to south-east. Length is measured over SMZ 3-9 and SMZ 3-7 only; adding SMZ 3-6 yields a length of $4\farcm5$ or 0.6 pc. Position refers to the K' source close to SMZ 3-9 A.

32: Faint knots to the north and south of a faint, slightly extended continuum source (regarded as the candidate driving source), but very uncertain. Position refers to the candidate driving source.

33: Knot SMZ 3-12 C together with the faint emission between C and A delineate a short, faint, well-collimated jet beam, which ends in a working surface outlined by knots A and B. Source of the flow is presumably located at the north-western end of the jet, close to knot C. Position refers to this north-western end. No counter flow detected.

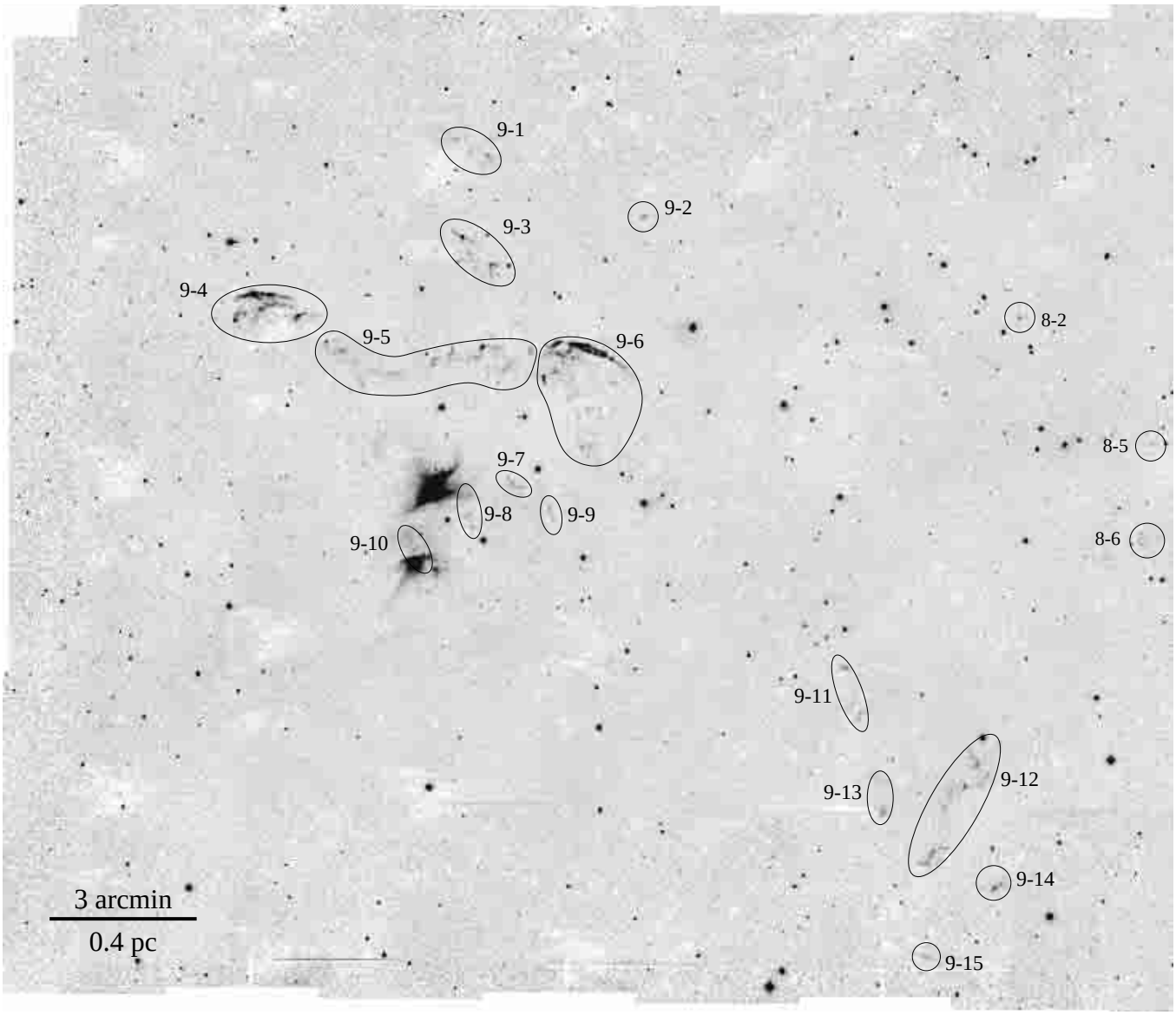

Fig. 11. H_2 features in Field 9. The figure shows the 2.12 μm narrow band image (not continuum subtracted) in linear intensity scaling. The size of the field is $24\farcm1 \times 20\farcm8$, centered on $\alpha = 5^h40^m15\fs0$, $\delta = -7°27'42''$ (J2000). North is up, east to the left.

34: Knots SMZ 3-13 A and B and possibly some more faint emission along their connecting line may delineate a short, well-collimated jet (very uncertain). Position refers to SMZ 3-13 A (no driving source identified).

35: Possible shock in flow from weak IRAS source 40″ north-east of SMZ 3-14; extremely uncertain. Position refers to H_2 feature SMZ 3-14.

36: 3 knots in a row: short, faint, collimated jet. Position refers to SMZ 3-15 A (no source identified).

37: Features in SMZ 3-17 define narrow, well-collimated jet. SMZ 3-16 A is a bright bow shock on jet axis. Source is presumably close to SMZ 3-17 A. Position refers to SMZ 3-17 A. No counter flow detected.

38: SMZ 4-2 and SMZ 4-3 define a faint, narrow, very well-collimated flow; SMZ 4-5 (and possibly SMZ 4-6 and SMZ 4-7) may form a terminating working surface. Position refers to the candidate driving source.

39: Very poorly-defined flow, very uncertain. Position refers to H_2 knot SMZ 4-7 (no source identified).

40: Either short, bright, narrow jet or tip of a bow shock in flow from IRAS 05331−0606 to the south-south-west; very uncertain. Position refers to H_2 knot SMZ 4-9 A.

41: SMZ 4-10 is presumably a bow shock in a flow from the north; very uncertain. Position refers to H_2 knot SMZ 4-10 A (no driving source identified).

42: SMZ 4-12 A is an apparently faint, narrow, very well-collimated jet beam, with the driving source at its eastern end. SMZ 4-12 B seems to be a bow shock ahead of this jet. SMZ 4-11 appears to delineate the counter flow, but is very faint. Position refers to the candidate driving source.

43: Filamentary structures forming bipolar bubble-like structures to the east and west of V 1296 Ori, possibly indicating a very poorly-collimated flow from that star. Position refers to the candidate driving source V 1296 Ori.

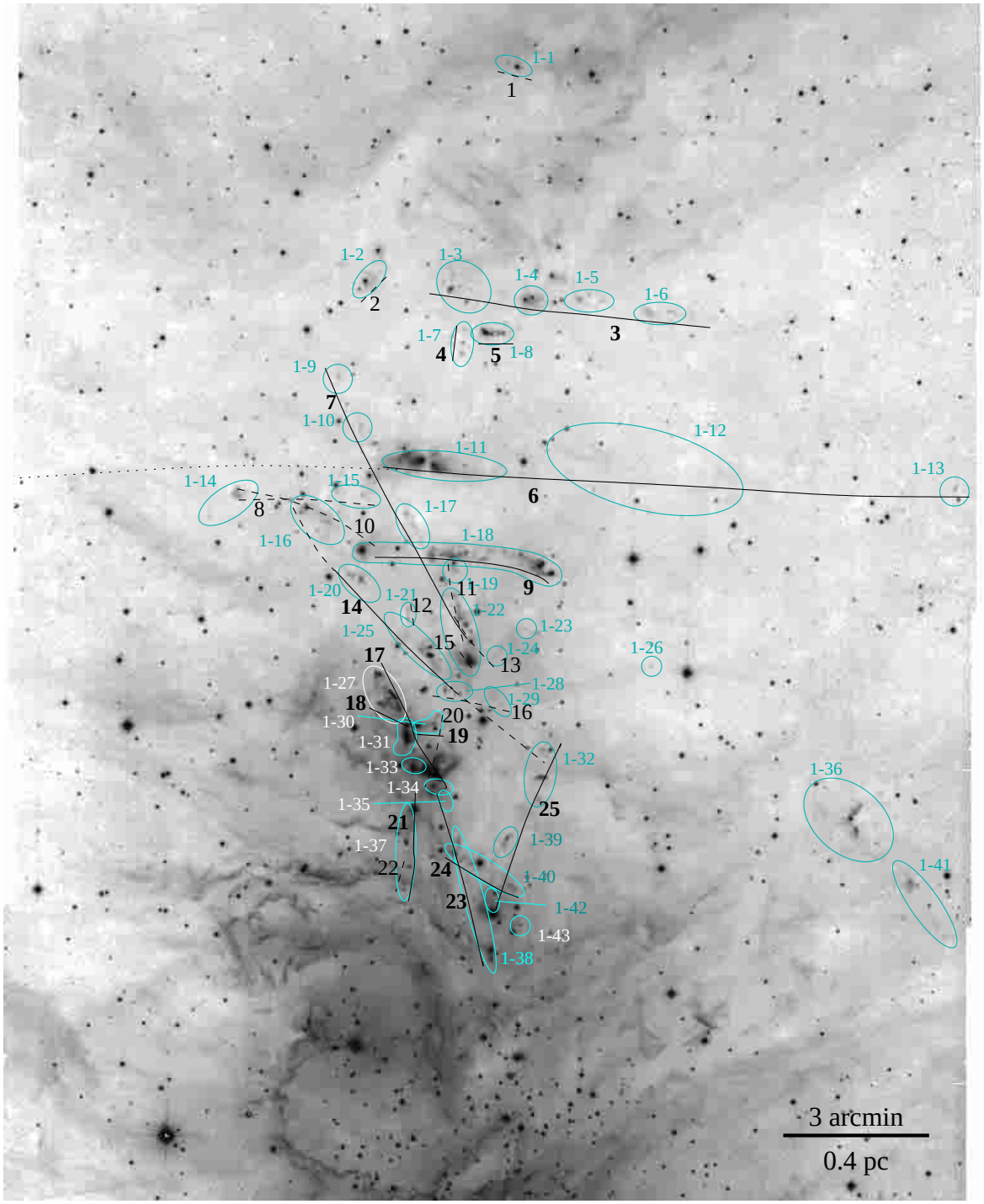

Fig. 12. Jets in Field 1 (the OMC-2/3 area). The figure shows the 2.12 μm narrow band image (not continuum subtracted) in logarithmic intensity scaling. The size of the field is $20\farcm3 \times 25\farcm1$, centered on $\alpha = 5^{\rm h}35^{\rm m}20\fs6$, $\delta = -5°06'20''$ (J2000). North is up, east to the left.

44: SMZ 5-3 seems to outline a flow from north-west, with knots A and B outlining the (apparently rather broad) flow itself, and feature C being a bow shock-like working surface. Position refers to knot A (no driving source identified).

45: Group of knots extending south from the candidate driving source (red, nebulous star north of SMZ 5-4 A/B); uncertain. SMZ 5-4 may also belong to the northern lobe of a large flow (**#49**) from the L 1641-N cluster. Position refers to the candidate driving source.

46: North-south bipolar H_2 and optical HH-flow from nebulous star. Knot B is very compact and may indicate a well-collimated jet; knot A is elongated in an east-west direction and may be a bow shock-like structure. Position refers to the candidate driving source.

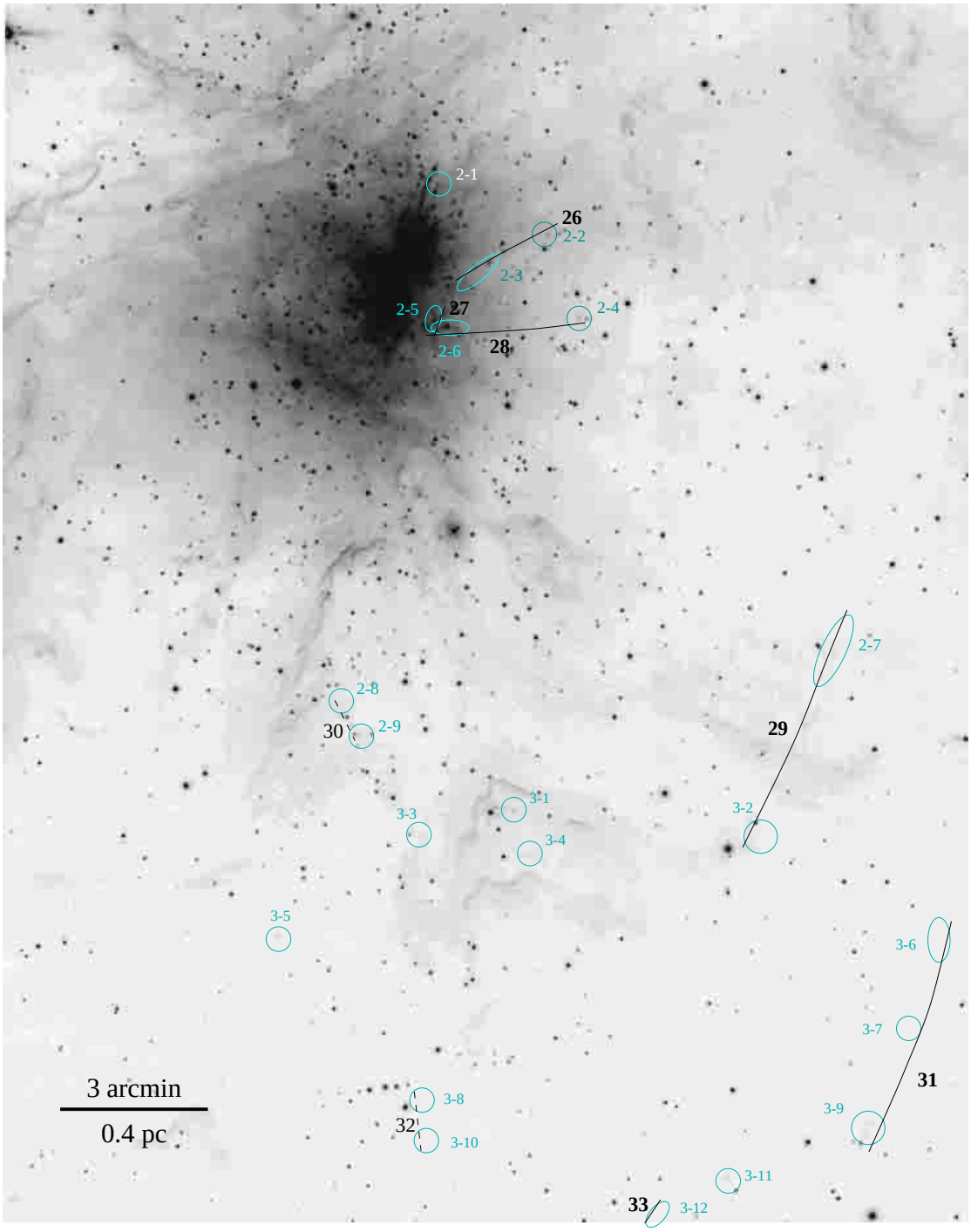

Fig. 13. Jets in Field 2 (the Orion Nebula area). The figure shows the 2.12 μm narrow band image (not continuum subtracted) in logarithmic intensity scaling. The size of the field is $19\farcm8 \times 24\farcm7$, centered on $\alpha = 5^{\rm h}35^{\rm m}07\fs5$, $\delta = -5°29'34''$ (J2000). North is up, east to the left.

47: SMZ 5-6 B may indicate faint, well-collimated jet beam. SMZ 5-6 A appears to be a bow shock in a flow from the direction of feature B. Position refers to knot SMZ 5-6 B.

48: SMZ 5-9 is a narrow, jet-like filament; connection with SMZ 5-19 is not clear, but there may be some more very faint emission between them. Position of the driving source is also not clear, but it may be located between SMZ 5-9 B and D, or to the south-west of SMZ 5-9 B, between SMZ 5-9 B and SMZ 5-19. Length of flow is measured over SMZ 5-9 only. Position refers to H_2 feature SMZ 5-9 D.

49: L 1641-N giant flow (Stanke et al. 1998, 2000). Only a small fraction of the northern lobe of the flow is detected in H_2 (SMZ 5-14 B, G, P (?), SMZ 5-8), but this lobe is traced by optical HH-objects over a length of more than 6 pc (Reipurth et al. 1998; Mader et al. 1999). The southern lobe detected in the infrared extends over 4 pc, but may continue further south, beyond the edge of the mosaic 6.

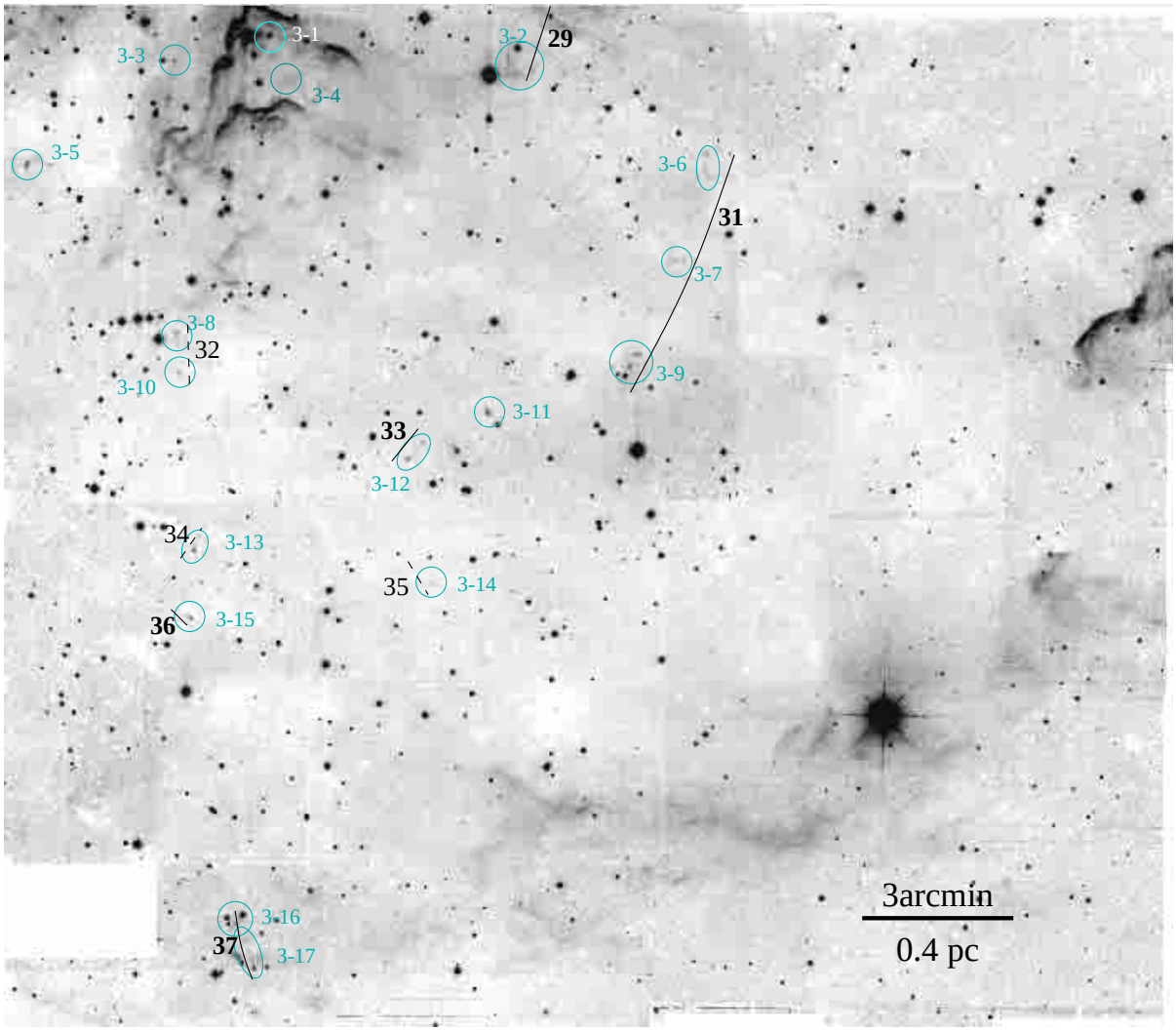

Fig. 14. Jets in Field 3 (the area south of the Orion Nebula). The figure shows the 2.12 μm narrow band image (not continuum subtracted) in linear intensity scaling. The size of the field is $23\farcm2 \times 20\farcm3$, centered on $\alpha = 5^{\rm h}34^{\rm m}38\fs3$, $\delta = -5°42'56''$ (J2000). North is up, east to the left.

Length given in table is measured over the H_2 features only, from SMZ 5-8 down to SMZ 6-16. Some other H_2 features north of the L 1641-N cluster (SMZ 5-1 and SMZ 5-4) may also belong to this flow. The H_2 features outline a rather broad path, but nevertheless, the flow appears to be rather well-collimated: the underlying flow is presumably narrower than the path seen in H_2 since the H_2 features are probably bow shocks and thus wider than the flow. The path also appears to show some bendings, perhaps indicating a time-varying direction of ejection. Position refers to the candidate driving source.

50: Short, roughly spindle-shaped flow. There is no driving source identified, but presumably it is located between SMZ 5-15 B and D. Position refers to point between SMZ 5-15 B and D.

51: Roughly east-west flow originating in millimetre source (Stanke et al., in prep.) between SMZ 5-16 A and B. SMZ 5-16 A, SMZ 5-12, and SMZ 5-11 form the eastern lobe of the flow; the counter flow is indicated by SMZ 5-16 B and possibly SMZ 5-19. Length is measured over SMZ 5-16, SMZ 5-12, and SMZ 5-11; total length of the flow may be about 2 pc, assuming it to be symmetric about its driving source. The morphology of SMZ 5-16 A and B seem to indicate that the flow here is interacting with the walls of its outflow cavity, possibly traced by some reflection nebulosity. SMZ 5-12 and SMZ 5-11 may be large bow shocks, and are also detected at optical wavelengths (Reipurth et al. 1998, Mader et al. 1999). Position refers to the candidate driving source.

52: Another possible large-scale flow from somewhere in the L 1641-N cluster, but very uncertain. Position refers to the centre of the cluster.

53: Short flow from the centre of the L 1641-N cluster. The jet beam itself is not visible, but SMZ 5-14 A1 is apparently a bright bow shock pointing away from the cluster centre (see also Stanke et al. 1998). Position refers to the candidate driving source, N1 of Chen et al. (1993).

54: Jet from an edge-on star/disk system. Position refers to the candidate driving source.

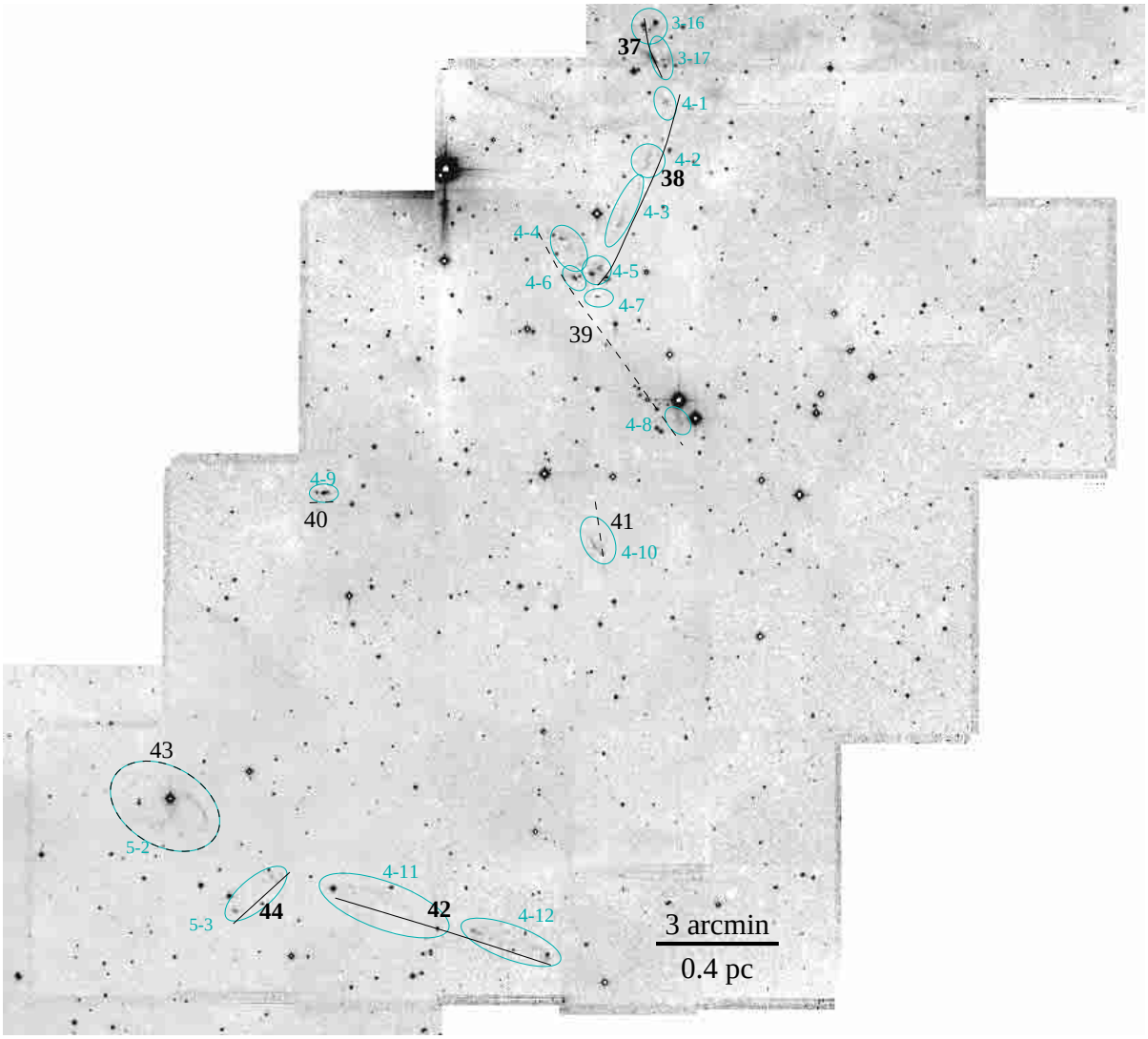

Fig. 15. Jets in Field 4. The figure shows the 2.12 μm narrow band image (not continuum subtracted) in linear intensity scaling. The size of the field is $27\farcm8 \times 25\farcm1$, centered on $\alpha = 5^h35^m12\fs8$, $\delta = -6°03'07''$ (J2000). North is up, east to the left.

55: HH 34 giant flow (Bally & Devine 1994; Devine et al. 1997; Eislöffel & Mundt 1997). Length is measured over the H_2 features as seen here only. HH 38/43 further to the north-west is also an H_2 bright object, but not on the mosaic presented here; total flow length is over 3 pc. The HH 34 inner jet (SMZ 5-21 B) is detected in the H_2 line here for the first time. The counter jet (SMZ 5-21 C) is detected for the first time at any wavelength. Position refers to the driving source.

56: Short, collimated flow. Position refers to the middle of the H_2 feature; no driving source is identified, but there are faint continuum sources at each end of the feature.

57: Two bright features with a morphology suggestive of small compact bow shocks in a bipolar configuration around BE Ori. The compactness of the bow shocks suggests the presence of a highly-collimated jet beam which is itself not visible as a H_2 jet or optical HH-jet (Mader et al. 1999). Position refers to the candidate driving source BE Ori.

58: Group of H_2 features in a roughly symmetric bipolar configuration around fan-shaped infrared source (candidate driving source). SMZ 5-27 A consists of two features, both suggestive of bow shocks heading away from the driving source. SMZ 5-27 B and C appear to be a symmetric pair of bow shocks at a greater distance from the driving source. Position refers to the candidate driving source.

59: The H_2 features SMZ 5-28 and SMZ 6-1 form the infrared counterpart to the north-south bipolar molecular outflow V 380 Ori NE (Levreault 1988; Morgan et al. 1991; Davis et al. 2000). These features indicate the presence of a well-collimated, precessing jet. Position refers to the candidate driving source.

60: Very poorly-defined flow, very uncertain. Position refers to the north-eastern knot of SMZ 6-7.

61: Flow consisting of faint features from H_2O maser/VLA source (Pravdo et al. 1985) coincident with SMZ 6-13. The morphology of this flow is not well defined; true shape is unclear, SMZ 6-11 or SMZ 6-6 may possibly also be part of

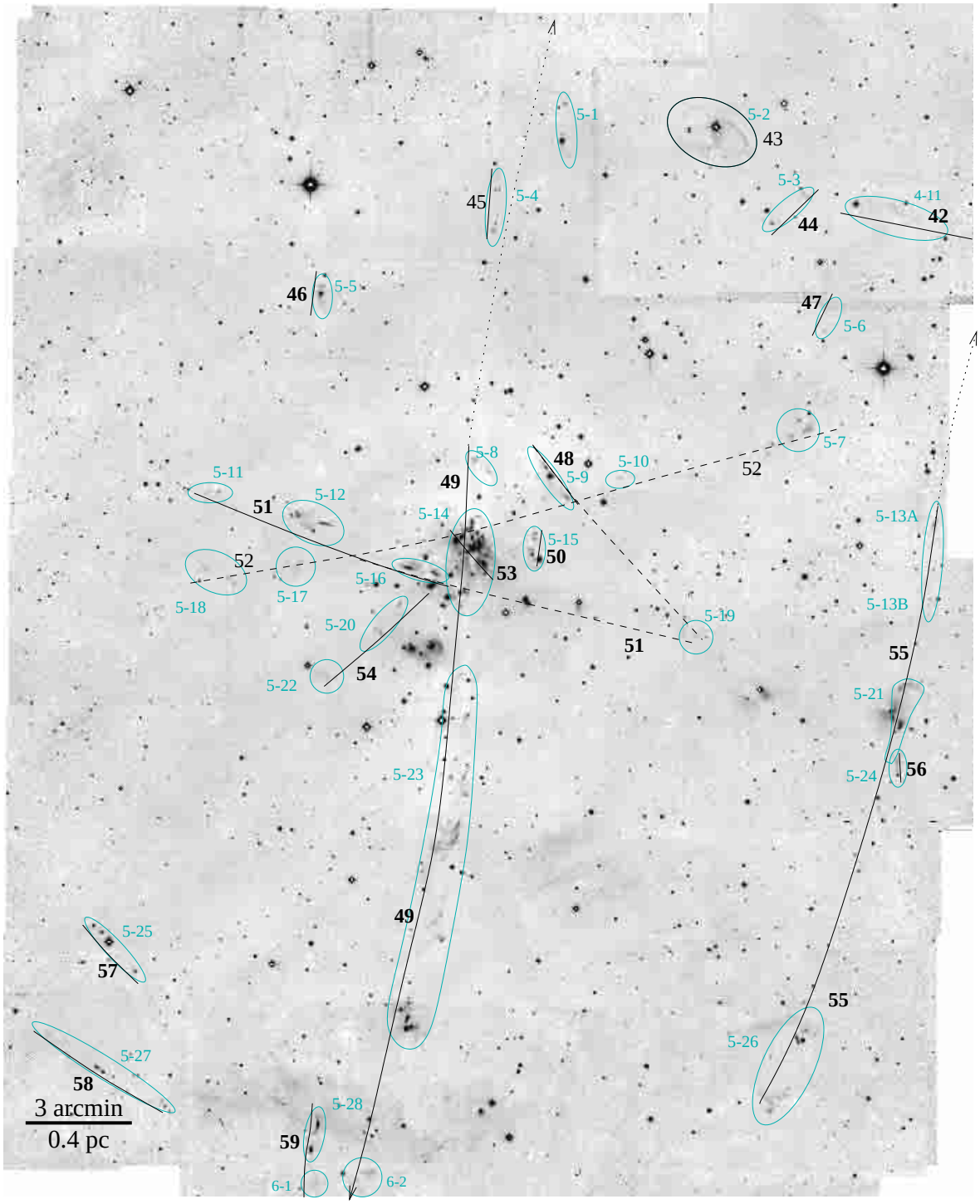

Fig. 16. Jets in Field 5 (the area around the L1641-N cluster) (the area around the L1641-N cluster, see also Stanke et al. 1998). The figure shows the 2.12 μm narrow band image (not continuum subtracted) in linear intensity scaling. The size of the field is $27\farcm6 \times 33\farcm8$, centered on $\alpha = 5^{\rm h}36^{\rm m}17\fs2$, $\delta = -6°23'31''$ (J2000). North is up, east to the left.

a flow from the same source. Position refers to the candidate driving source.

62: This flow is almost certainly not real. On the one hand, the H_2 and K' data alone suggest that there may be a well-collimated flow from a compact source (partly continuum, partly H_2 line emission) at the given position. However, this source is coincident with the tip of the very bright HH-object HH 1, and the continuum emission is presumably emission from other H_2 lines in the K' filter, and the H_2 feature SMZ 6-10 is presumably some part of the HH 1/2 flow. This conclusion however is based on optical data, although based on the infrared data alone, one would have to identify this as a likely jet. Thus we list it as a candidate flow here, albeit a very uncertain one.

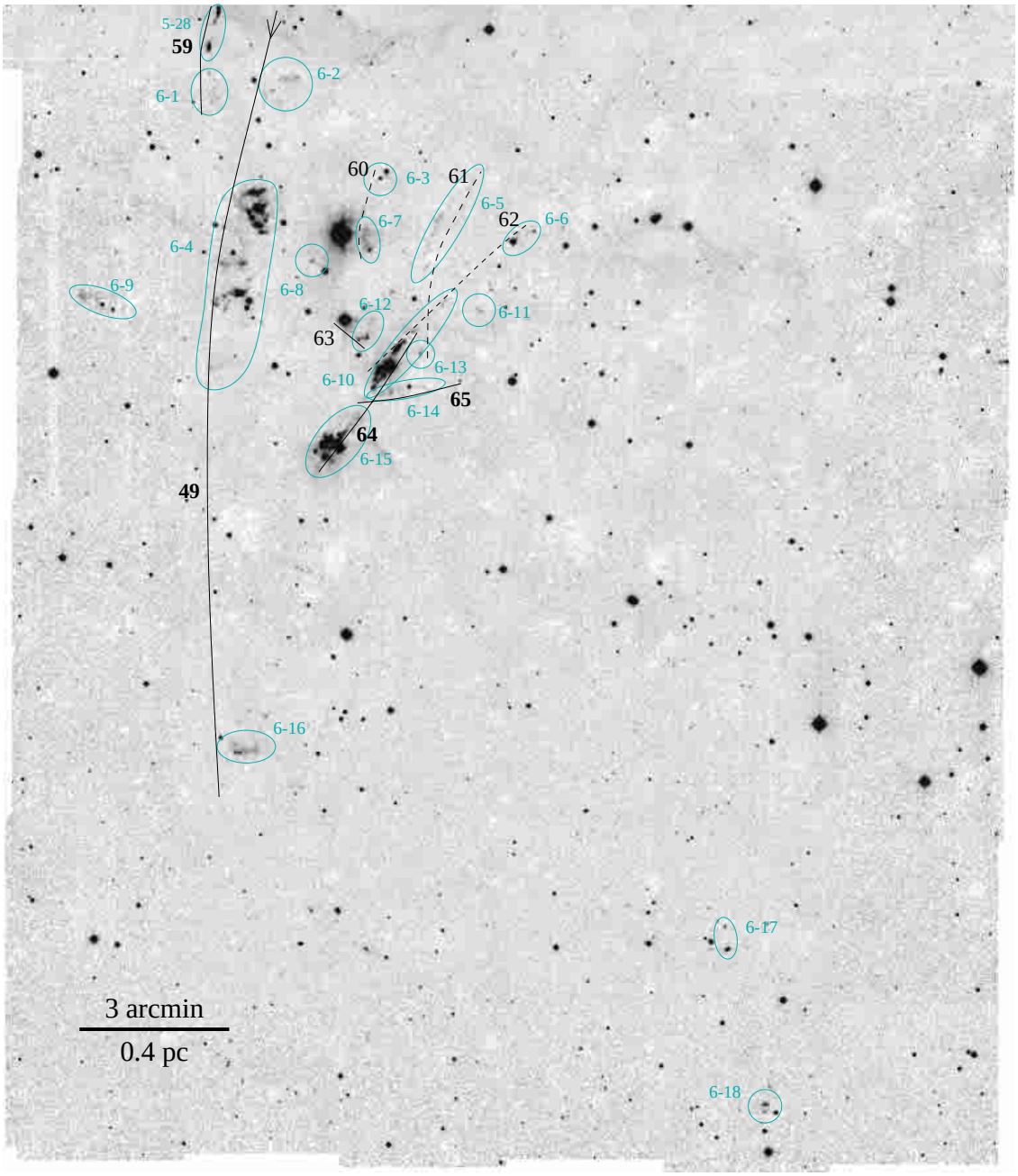

Fig. 17. Jets in Field 6 (the HH 1/2 and V 380 Ori area). The figure shows the 2.12 μm narrow band image (not continuum subtracted) in linear intensity scaling. The size of the field is $20\farcm3 \times 23\farcm5$, centered on $\alpha = 5^h36^m11\fs2$, $\delta = -6°50'02''$ (J2000). North is up, east to the left.

63: Several H_2 and optical HH-knots associated with reflection nebulosity suggesting a flow cavity from star N^3SK50 and a rather poorly-collimated flow through the cavity (e.g., Davis et al. 1994; Corcoran & Ray 1995). No counterflow detected. Position refers to the candidate driving source, N^3SK50.

64: HH 1/2 outflow system. SMZ 6-10 C indicates a very well-collimated jet beam, which flows through an illuminated cavity seen as conical reflection nebula. SMZ 6-10 B appears to delineate the interaction of a poorly-collimated flow component with the wall of the cavity. SMZ 6-10 A is part of the bow shock HH 1. SMZ 6-10 D and E seem to indicate a continuation of the flow beyond HH 1, or may belong to a different flow. In the counter lobe, only the bow shock HH 2 (SMZ 6-15) is seen. Position refers to the presumed driving source, HH 1/2 VLA1.

65: Faint, well-collimated H_2/HH flow (e.g., Bohigas et al. 1985; Strom et al. 1985; Reipurth et al. 1993). No counterflow detected. Position refers to the candidate driving source, HH 1/2 VLA2.

66: All features are located along a rough line, but may also belong to individual, unknown flows. No source is identified. Position refers to H_2 feature SMZ 7-2 A.

67: HH 43/38/64 giant flow (see Stanke et al. 2000). Well-collimated, but apparently rather broad jet. The north-western lobe is probably even longer than seen

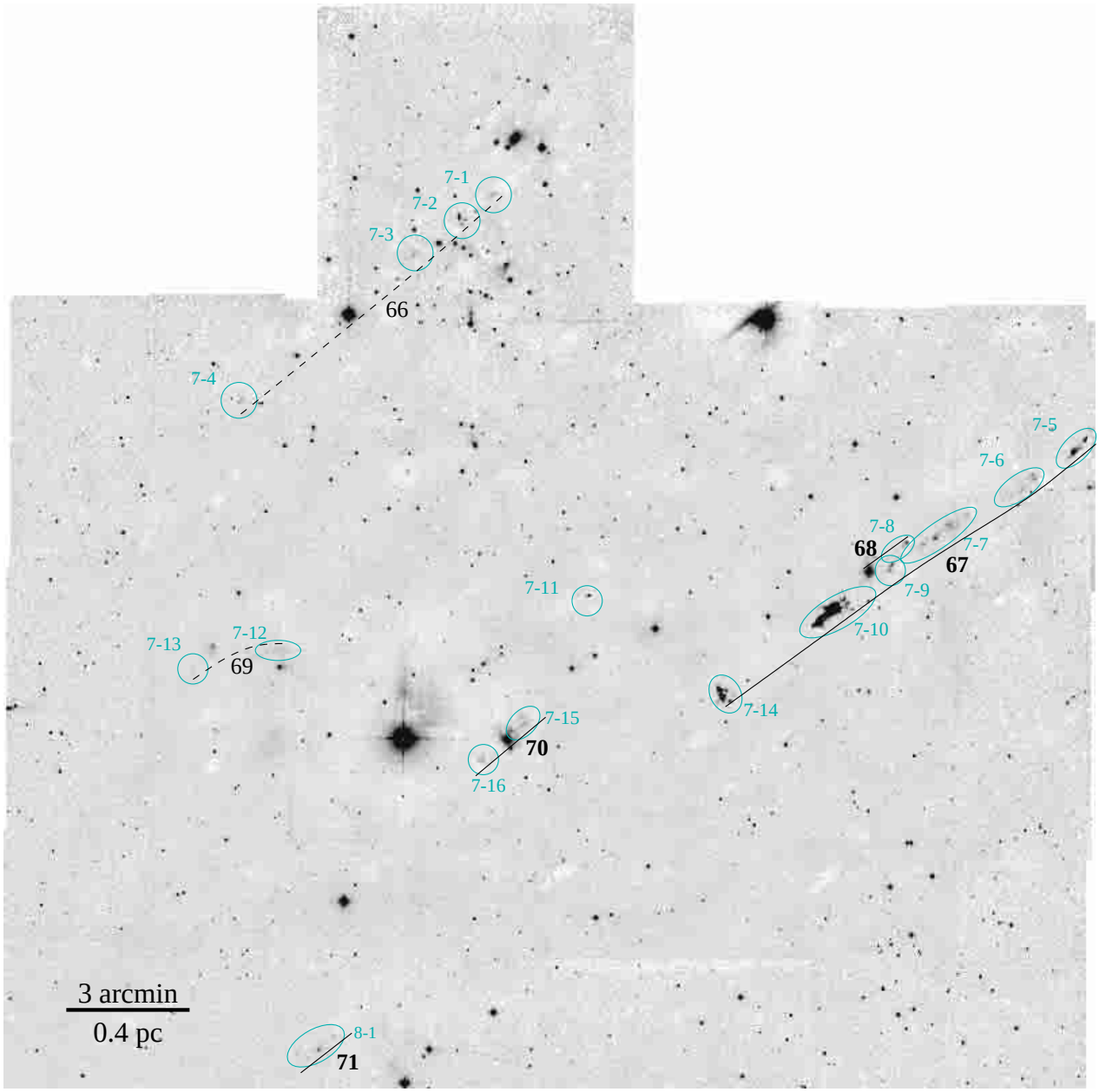

Fig. 18. Jets in Field 7 (the L1641-C and HH 43 area). The figure shows the 2.12 μm narrow band image (not continuum subtracted) in linear intensity scaling. The size of the field is $26\farcm7 \times 27\farcm5$, centered on $\alpha = 5^h38^m39\fs0$, $\delta = -7°08'35''$ (J2000). North is up, east to the left.

here. Position refers to the presumable driving source, HH 43 MMS1.

68: Bow shock in jet from HH 43 IRS1, filament (jet beam?) extending back from bow shock towards IRS. The supposed jet direction appears to be perpendicular to the dark lane intersecting the HH 43 reflection nebulosity. No counter flow detected. Position refers to the presumed driving source, HH 43 IRS1.

69: Some very weak H_2 features close to a nebulous continuum source. The morphology of the flow (which is itself very uncertain) is only very poorly constrained. Position refers to the candidate driving source.

70: Short, probably well-collimated H_2 and HH-flow from HBC 491 (Strom et al. 1986). The reflection nebulosity associated with this star suggests the presence of an outflow cavity. Position refers to the apparent driving source, HBC 491.

71: Faint H_2 knots distributed in a roughly bipolar configuration around a very weak infrared continuum source. The compactness of knots A and B may suggest a well collimated flow. Position refers to the presumed driving source, the nebulous infrared source.

72: Jet from Haro 4-255 FIR source. Well-collimated jet beam (SMZ 8-4 I, G) terminates in bow shock-like working surface (SMZ 8-4 A; see also Davis & Eislöffel 1995). The association of SMZ 8-2 and SMZ 8-7 with this flow is uncertain. Length of the flow given here is measured over SMZ 8-4 only. Position refers to apparent driving source.

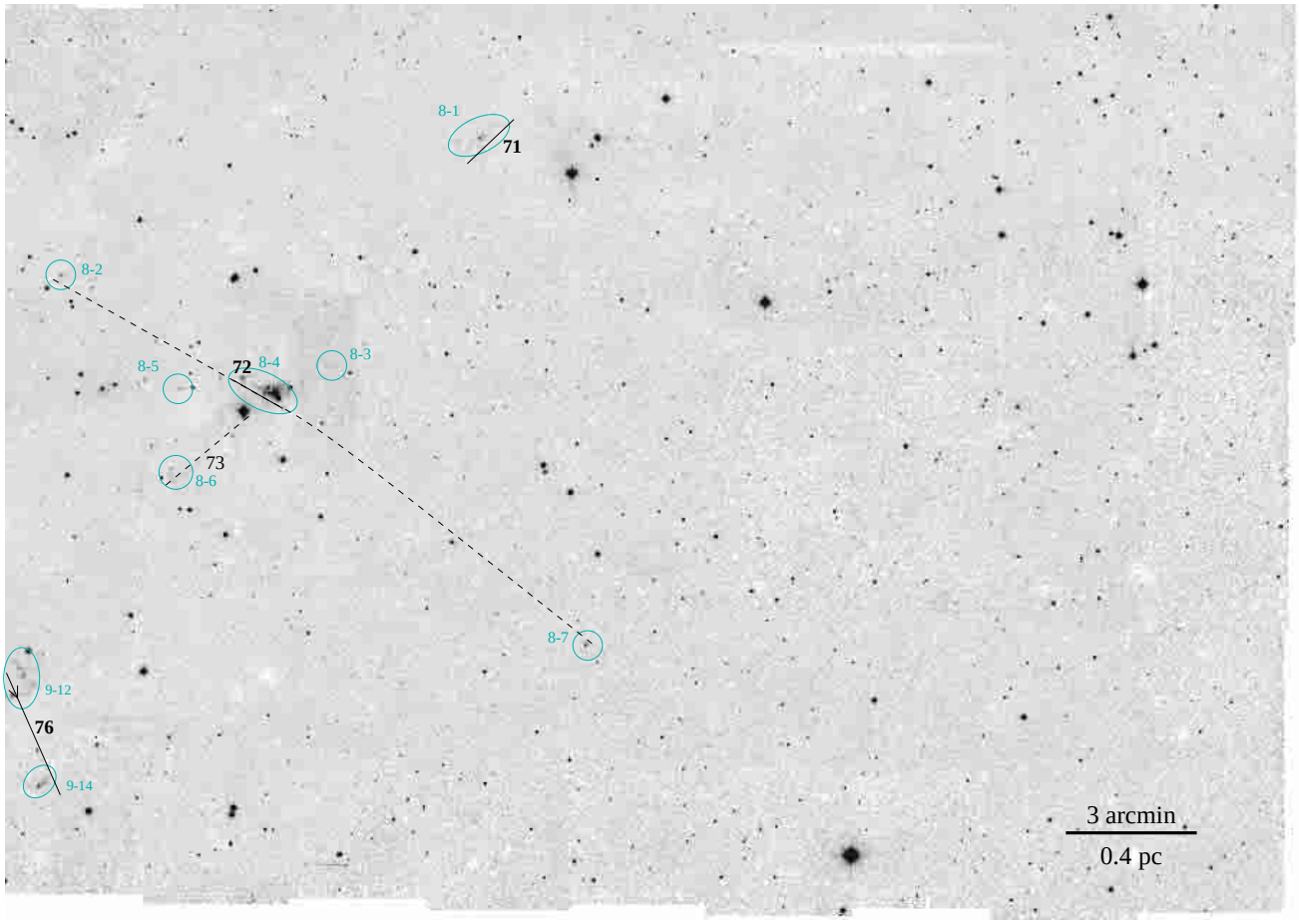

Fig. 19. Jets in Field 8. The figure shows the 2.12 μm narrow band image (not continuum subtracted) in linear intensity scaling. The size of the field is $29\farcm3 \times 21\farcm1$, centered on $\alpha = 5^h38^m44\fs0$, $\delta = -7°27'43''$ (J2000). North is up, east to the left.

73: The T Tauri star Haro 4-255 drives a well-collimated HH-jet (Aspin & Reipurth 2000), which terminates in a bow shock which is also detected as H_2 feature (SMZ 8-6). However, based on the H_2 data alone, this flow would not have been recognised, and is thus listed as an uncertain detection only. Position refers to the driving source, Haro 4-255.

74: H_2 knots distributed in a roughly symmetric bipolar configuration around a very weak K' continuum source. The H_2 features appear to outline a pair of bow shocks from this infrared source. The flow morphology is only very poorly constrained. Position refers to the apparent driving source.

75: Group of H_2 features possibly outlining a flow from one of the K' continuum sources associated with SMZ 9-3 A and SMZ 9-3 B. Alternatively, SMZ 9-3 may be part of the giant flow from L 1641-S3 MMS1 (**#76**). Position refers to point between SMZ 9-3 A and B.

76: L 1641-S3 giant flow (see Stanke et al. 2000 for a detailed discussion). Either a rather poorly-collimated or a strongly-bending flow from L 1641-S3 MMS1. The counter flow (features SMZ 9-11, SMZ 9-12, SMZ 9-13, SMZ 9-14, SMZ 9-15) presumably extends over a larger distance as seen here. Position refers to the apparent driving source.

5.3. Limitations and errors

The identification of the jets, as well as the measurement of their properties (the location of the jet, its position angle, its length, and its H_2 brightness or luminosity), are all subject to errors and uncertainties, which we will now discuss.

5.3.1. The jet sample

The H_2 survey covers a large area of a molecular cloud with a more or less uniform sensitivity and angular resolution, thus ensuring that features with similar apparent brightness and morphology can be detected with the same likelihood throughout the entire survey field. The most notable exception are areas affected by strong nebulosity, in particular the Orion Nebula area, which will thus be excluded from statistical investigations in the subsequent papers, as noted previously.

The large variety in the morphology of the H_2 features, ranging from large, extended, filamentary features to compact or even unresolved knots, makes it difficult to give a definite detection threshold in terms of surface brightness or total flux for the H_2 features. This problem not only affects individual H_2 features, but also entire flows, and the detection of flows thus depends on the brightness or H_2 luminosity and for a given

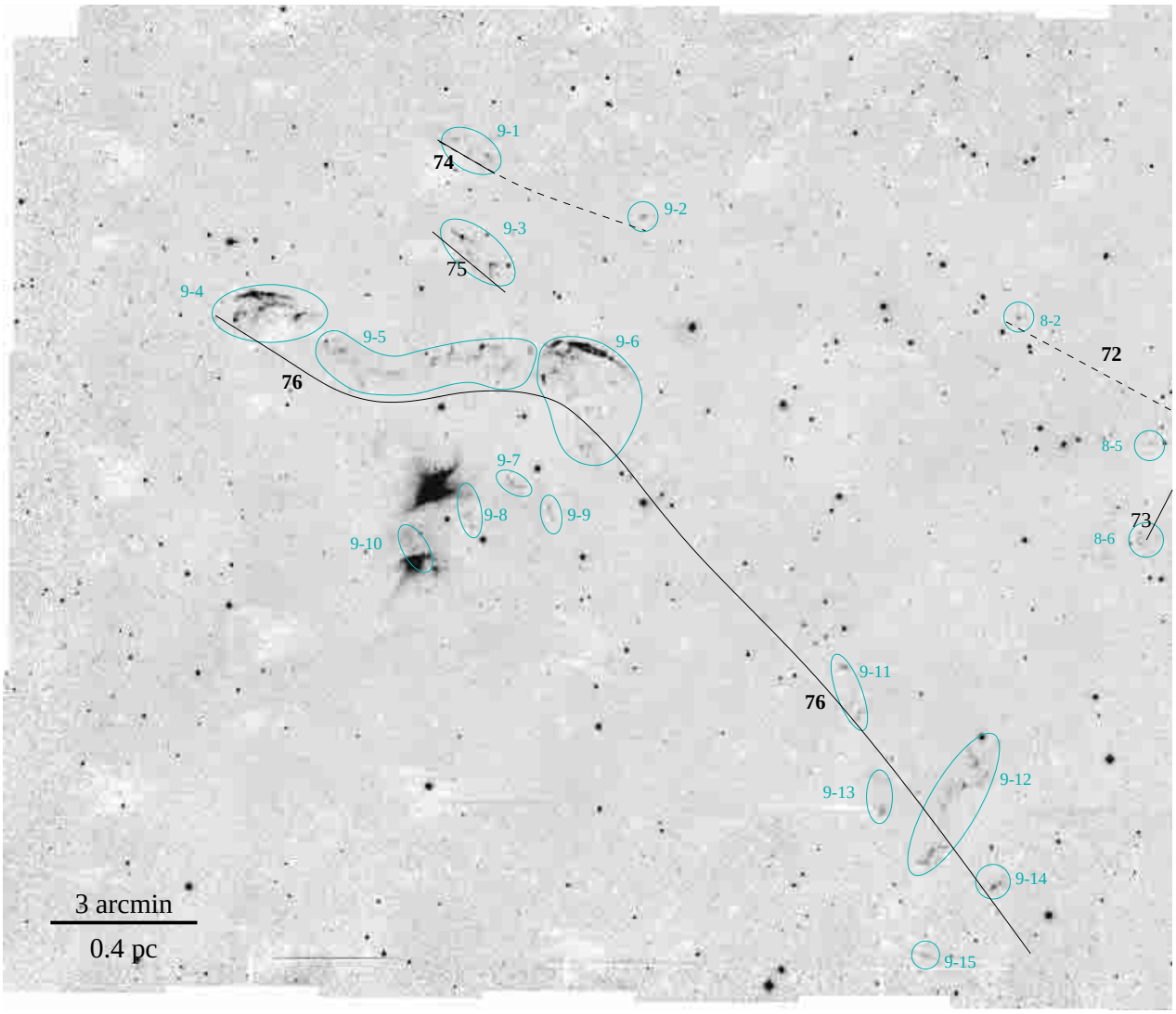

Fig. 20. Jets in Field 9. The figure shows the 2.12 μm narrow band image (not continuum subtracted) in linear intensity scaling. The size of the field is 24.′1 × 20.′8, centered on $\alpha = 5^h40^m15.^s0$, $\delta = -7°27'42''$ (J2000). North is up, east to the left.

brightness, the flow morphology. This is different from samples of stars, for example, which for a given data set are either detected or not, depending on their brightness alone.

The implication is that the variety in flow morphologies makes the identification of flows a somewhat subjective process. Some basic rules were followed as far as possible (e.g., two adjacent but otherwise isolated knots were not regarded as a flow, although they might form one), but the identification of flows often involved case-by-case decisions which are impossible to quantify in any reasonable way. The division of flows into "certain" and "uncertain" groups reflects this difficulty, and some of the flows identified in this work might later on turn out not to form a flow as suggested here, but be found to belong to other systems. However, this is a general problem in the study of outflows, and by no means restricted to our survey alone. A good example of how wrong previously determined flow groupings can be is given by the HH 43/38/64 flow, for which the new data obtained during the present H_2 survey suggested a greatly revised picture (Stanke et al. 2000).

In summary then, it is not possible to derive a sample of jets from the survey data on the basis of well-defined criteria, such as, for example, a flux-limited sample, despite the survey being unbiased and covering the survey region completely and uniformly. This limitation has to be kept in mind when statistical statements about the jet sample are made.

5.3.2. Jet location

For a reasonable fraction of the jets, a candidate driving source is either obvious or strongly suggested (Stanke 2000). The positions of these sources may be accurate to a few arcseconds if seen in near-infrared, or less so if only IRAS positions are known. For jets without an identified driving source, a characteristic position is given (e.g., a bright knot perhaps), but this position might be wrong by as much as the full flow length in some cases. Generally however, jets without driving source identification are relatively short, implying that the errors in the jet location will not be larger than a few arcminutes at most.

Table 3. List of H_2 flows.

Flow #	RA (J2000)	Dec (J2000)	H_2 features SMZ	Length	(pc)	PA	$L_{2.12}$ $10^{-4}\,L_\odot$	CS core
			Field 1					
1	5 35 19.1	−4 55 46	1-1	0.′34	0.05	68	1.3	—
2	5 35 31.5	−5 00 21	1-2	0.′43	0.06	−41	1.9	4
3	5 35 18.2	−5 00 33	1-4, 1-5, 1-6; 1-3(?)	5.′23	0.70	84	31.5	3
4	5 35 23.4	−5 01 31	1-7	0.′53	0.07	−4	3.8	4
5	5 35 22.4	−5 01 16	1-8	0.′42	0.05	90	58.6	4
6	5 35 26.4	−5 03 54	1-11, 1-12, 1-13	11′	1.43	88	15.7	—
7	5 35 27.8	−5 05 00	1-9, 1-10, 1-17, 1-22; 1-24(?)	6′	0.80	29	22.0	—
8	5 35 31.5	−5 04 39	1-15, 1-14	2.′83	0.37	−89	11.3	—
9	5 35 26.2	−5 05 46	1-18 A–G; H(?)	2.′62	0.34	81	195.2	—
10	5 35 31.4	−5 05 48	1-18 H, 1-16, 1-14(?)	2′	0.26	66	37.8	—
11	5 35 23.5	−5 06 11	1-19; 1-22(?)	0.30(?)	0.05(?)	∼0	10.1	—
12	5 35 27.4	−5 07 07	1-21	0.′23	0.03	7	2.2	8
13	5 35 23.1	−5 07 09	1-22 A, B; 1-22 E (?); 1-24(?)	1.′08	0.14	45	10.7	8
14	5 35 28.1	−5 07 20	1-20, 1-25, 1-28(?), 1-29(?), 1-32 A(?), 1-16(?)	3.′43	0.48	45	31.5 (79)	8
15	5 35 23.3	−5 07 32	1-22 F	0.′76	0.10	∼51	3.6	8
16	5 35 24.3	−5 08 33	1-28, 1-29	1.′33	0.17	77	8.8	8
17	5 35 27.5	−5 09 37	1-27 A, C, D, 1-34, 1-31 C, D(?)	2.′84	0.37	31	110.2	11
18	5 35 27.5	−5 09 17	1-27 B, E	0.′75	0.10	56	22.0	11
19	5 35 26.7	−5 09 24	1-30 B-A	0.′38	0.05	−83	7.6	11
20	5 35 25.5	−5 09 41	1-30 C, D, (A); 1-33 A, C	1.′25	0.16	−19	6.3	11
21	5 35 27.2	−5 11 11	1-37 E...C	1.′70	0.22	−1	44.1	11
22	5 35 27.2	−5 12 32	1-37 B-C	0.′62	0.08	−14	7.6	13
23	5 35 22.8	−5 11 50	1-38, 1-35 (?)	3.′60	0.47	18	51.6	11
24	5 35 23.3	−5 12 03	1-40	1.′52	0.20	61	25.2	11
25	5 35 21.4	−5 13 14	1-42, 1-39, 1-32	3.′33	0.44	−20	40.3	15
			Field 2					
26	5 35 10.9	−5 23 12	2-3, 2-2	2.′58	0.34	−55	36.5	—ON
27	5 35 11.6	−5 23 41	2-5 (C ?)	0.′22	0.03	−19	40.9	—ON
28	5 35 10.9	−5 23 46	2-6; 2-5 C(?); 2-4(?)	0.′38	0.05	89	63.0	—ON
29	5 34 40.7	−5 31 44	2-7, 3-2	5′	0.66	−23	9.5	
30	5 35 18.2	−5 31 42	2-8, 2-9	0.′90	0.12	25	1.1	—
			Field 3					
31	5 34 35.3	−5 39 59	3-9, 3-7; 3-6(?)	2.′42	0.31	−23	2.8	
32	5 35 11.3	−5 39 39	3-8, 3-10	0.′90	0.12	3	1.1	—
33	5 34 51.6	−5 41 31	3-12	0.′57	0.07	−42	1.6	—
34	5 35 09.7	−5 43 45	3-13	0.′37	0.05	−25	0.9	
35	5 34 50.7	−5 44 21	3-14	0.′7(?)	0.8(?)	30(?)	0.4	51
36	5 35 09.9	−5 45 06	3-15	0.′18	0.02	58	1.1	
37	5 35 04.4	−5 52 01	3-16 (A), 3-17	1.′20	0.16	15	10.4	—
			Field 4					
38	5 35 08.8	−5 55 53	4-2, 4-3, 4-5; 4-1(?)	3.′25	0.42	−24	7.9	56
39	5 35 10.7	−5 57 37	4-4, 4-6, 4-5(?), 4-7, 4-8	5.′51	0.71	34	10.1	57
40	5 35 36.9	−6 02 29	4-9	0.′25	0.03	−89	6.7	—
41	5 35 09.7	−6 03 53	4-10	>0.′5	>0.07	∼18	2.8	—
42	5 35 21.9	−6 13 06	4-11, 4-12	5.′33	0.69	71	2.5	
			Field 5					
43	5 35 51.9	−6 10 01	5-2	2′	0.26	56	2.5	—
44	5 35 41.8	−6 11 55	5-3	1.′50	0.20	−49	1.8	—
45	5 36 17.1	−6 11 10	5-4	1.′67	0.22	1	1.3	—
46	5 36 36.8	−6 14 58	5-5	0.′66	0.09	1	1.3	65
47	5 35 37.9	−6 15 06	5-6	0.′83	0.11	−25	0.8	—
48	5 36 10.0	−6 20 02	5-9; 5-19(?)	1.′40	0.18	38	3.8	—
49	5 36 19.6	−6 22 13	5-14, 5-8, 5-23, 6-2, 6-4, 6-16; 5-1(?), 5-4(?)	34′	4.43	−6	192.1	67
50	5 36 12.1	−6 21 58	5-15	0.′68	0.09	−8	4.2	—
51	5 36 24.8	−6 22 42	5-16, 5-12, 5-11; 5-19(?)	7.′24	0.94	71	23.3	69
52	5 36 19.1	−6 22 09	5-7, 5-10, 5-17, 5-18	17.′4	2.20	−74	5.6	67
53	5 36 18.8	−6 22 10	5-14 A1, C, Q	1.′15	0.15	43	10.3	67

Table 3. continued.

Flow #	RA (J2000)	DEC (J2000)	H_2 features SMZ	Length	(pc)	PA	$L_{2.12}$ $10^{-4}L_\odot$	CS core
			Field 5					
54	5 36 23.5	−6 23 11	5-20, 5-22	3.′05	0.40	−42	2.0	69
55	5 35 29.7	−6 26 59	5-21, 5-13, 5-26	17.′5	2.28	−15	18.9	71
56	5 35 29.8	−6 28 07	5-24	0.′50	0.065	4	1.5	—
57	5 36 59.8	−6 33 27	5-25	1.′84	0.24	43	3.3	86
58	5 37 00.2	−6 37 10	5-27	4.′17	0.54	59	4.4	
59	5 36 36.4	−6 38 58	5-28, 6-1	2.′17	0.28	1	12.6	89
			Field 6					
60	5 36 23.6	−6 43 07	6-3, 6-7	1.′50	0.20	−10	3.1	—
61	5 36 18.9	−6 45 21	6-5, 6-13	3.′10	0.40	−9	2.8	—
62	5 36 20.2	−6 45 06	6-6, 6-10 B, A, D, E	4.′17	0.54	−45	23.9	91
63	5 36 25.0	−6 44 42	6-12	0.′60	0.08	41	2.9	91
64	5 36 22.8	−6 46 07	6-10, 6-15	3′	0.39	−33	100.8	92
65	5 36 22.9	−6 46 10	6-14	1.′38	0.18	−83	1.3	92
			Field 7					
66	5 38 48.2	−7 01 53	7-1, 7-2, 7-3; 7-4(?)	2.′63	0.34	−51	3.1	95
67	5 37 57.6	−7 07 00	7-5, 7-6, 7-7, 7-9, 7-10, 7-14	11.′17	1.45	−54	172.6	97
68	5 38 07.3	−7 08 31	7-8	1.′18	0.15	−50	1.9	98
69	5 39 11.8	−7 10 35	7-12, 7-13	2.′63	0.34	∼−75	0.8	—
70	5 38 42.7	−7 12 44	7-15, 7-16	1.′67	0.21	−46	3.3	—
			Field 8					
71	5 39 00.8	−7 20 23	8-1	0.′93	0.12	−52	0.9	111
72	5 39 19.6	−7 26 18	8-4, 8-2(?), 8-7(?)	1.′25	0.16	63	13.2	117
73	5 39 22.2	−7 26 45	8-6	2.′33	0.30	−47	0.6	117
			Field 9					
74	5 40 25.3	−7 20 28	9-1, 9-2(?)	1′	0.13	53	2.1	
75	5 40 24.6	−7 22 31	9-3	1.′47	0.19	46	5.7	
76	5 39 55.1	−7 30 27	9-4, 9-5, 9-6, 9-11, 9-12, 9-13, 9-14, 9-15; 9-3(?)	20.′5	2.7	∼50	138.5	123
HH 212	5 43 51.1	−1 03 01		3.′9	0.51		69	
HH 211	3 43 56.6	32 00 53		1.′8	0.157		34	

In our subsequent analysis papers, the jet positions will at first be discussed only with respect to their general location within the molecular cloud, and thus uncertainties in the position of the associated driving source will not affect the conclusions at all. We will also discuss the possible association of the jets with the molecular cloud cores in the survey area, e.g., the CS cores of Tatematsu et al. (1993). These cloud cores have sizes typically on the order of one to a few arcminutes and positional accuracies on the order of ∼10″, and thus for jets with a well-identified driving source, their positional uncertainties will not be a major problem. However, in some cases of jets without such an identification, the positional uncertainty might be big enough to lead to an error in making an association or non-association between a jet and a cloud core. Our assessment is that this will be the case for a handful at most, and thus our conclusions are unlikely to be grossly affected.

5.3.3. Jet position angle

The position angle of a jet is fairly easily derived and reasonably well constrained (to within a few degrees), even for the more poorly defined flows. Only in one flow (**#76**) there is evidence for a major (i.e., more than 10°) change of flow direction, making it difficult to give an unambiguous flow position angle. In our analyses, flow position angles are discussed only with respect to their general, approximate alignment or misalignment with a given orientation, and uncertainties in the jet position angle of a few degrees will not be important.

5.3.4. Jet length

At face value, the length of a jet is also relatively easily derived. Measurement errors will be at most on the order of a few arcseconds due to possible errors in the pixel scale or the positional registration of the individual exposures making up a mosaic. Since the typical extent of the jets is on the order of an arcminute or more, these errors will be negligible.

However, a number of other uncertainties exist which will in general lead to systematic underestimates in jet lengths. First, the inclination of the jets with respect to the line of sight is not known, and thus only the projected length of a jet can be measured. However, for a random sample of jet orientations,

we found the mean scaling factor between projected and true jet length to be 0.785[2], thus for the entire sample of jets or subsamples of it the average length would not be dramatically underestimated. Second, the full extent of the flow may not in fact be observed: extinction may hide parts of the flow; the jet may not be visible over some part of its extent in H_2 emission; or the jet may extend beyond the observed area. For example, the HH 34 giant flow (H_2 flow **#55**) is known to extend over a total length of ~3 pc (Bally & Devine 1994; Devine et al. 1997; Eislöffel & Mundt 1997), but only part of its northern lobe lies within the area covered by our H_2 survey. Thus the length given here is only 2.3 pc. Similarly, the L1641-N giant flow (H_2 flow **#49**) is listed with a length of 4.4 pc. However, only a small part of its known northern lobe is seen in the H_2 survey; the rest is too faint, or again out of the survey area. Including the chain of Herbig-Haro objects which outline the northern lobe (Reipurth et al. 1998; Mader et al. 1999), the total flow length is at least 10 pc. Another example is the H_2 flow **#51**, of which only one lobe is seen. This outflow presumably has a counterlobe located within the survey area but undetected, and its length is probably closer to 2 pc than the 0.9 pc given here.

In our analyses, we restrict ourselves to discussions of only general trends in jet length when flows are grouped into broad bins, as a function of driving source luminosity, for example. The uncertainties which have been noted here should, to first order, affect these groups to similar extents, and thus will not greatly affect the conclusions drawn.

5.3.5. Jet brightness/luminosity in H_2

Determining and interpreting the H_2 brightness of the jets are subject to various sources of uncertainty. First, basic photometric errors must be considered. While our photometric calibration in general yielded results which are in reasonable agreement with previous work, some of the observations were made under non-photometric conditions. However, each survey field was covered at least once under photometric conditions, and thus we were able to provide a bootstrap correction to the non-photometric data when constructing the mosaics. Typical residual errors are on the order of 10%.

The generally extended morphology of the H_2 features introduces another uncertainty, as there can be significant variations in the measured fluxes caused by faint emission surrounding the features or by intensity variations in the background, depending on the aperture size used to measure the flux. For more compact features, this uncertainty may be on the order of 10%, while for low surface brightness, very extended features, the uncertainties may be much larger. In total then, we estimate errors in the raw H_2 photometry to be on the order of 10–30% for most H_2 features.

[2] If α is the angle between the jet axis and the line of sight, then the projected length of the jet is $L_\mathrm{p} = L_0 \cdot \sin\alpha$. The probability that the jet is points into a solid angle element $\mathrm{d}\Omega = \sin\alpha \cdot \mathrm{d}\alpha \cdot \mathrm{d}\phi$ is $\mathrm{d}P = \mathrm{d}\Omega/\Omega$. The average projected jet length of a randomly oriented jet sample is then $\overline{L_\mathrm{p}} = \int_\Omega L_\mathrm{p}\mathrm{d}\Omega / \int_\Omega \mathrm{d}\Omega = \int_0^{2\pi}\int_0^{\pi} L_0 \sin^2\alpha \,\mathrm{d}\alpha\,\mathrm{d}\phi / \int_0^{2\pi}\int_0^{\pi} \sin\alpha\,\mathrm{d}\alpha\,\mathrm{d}\phi = L_0 \cdot [\alpha/2 - 1/4 \sin 2\alpha]_0^{\pi} / [-\cos\alpha]_0^{\pi} = L_0 \cdot \pi/4 = 0.785 \cdot L_0$.

Unknown extinction is the major problem in converting the measured H_2 fluxes to their intrinsic equivalents, in order to determine the true H_2 luminosity of the jets. Extinction can vary considerably from flow to flow and also along a given flow as it breaks out of a dense cloud core. For example, in the prototypical young H_2 flow, HH 212, the estimated extinction ranges from $A_V \sim 20$ mag for the innermost knots to $A_V \sim 2$ mag for the outer bow shocks (Zinnecker et al. 1998), and the measured 2.12 μm luminosity of $0.0053\,L_\odot$ must be multiplied by a factor of more than 3 to yield the intrinsic 2.12 μm luminosity of $0.018\,L_\odot$. In the case of the infrared jet emanating from the Class 0 protostar HH 24 MMS, Bontemps et al. (1996b) apply an an extinction correction of $A_V \sim 50$ mag, or a factor of roughly 100 at 2.12 μm.

Some of our flows appear to be deeply embedded, but on the other hand, there are certainly some H_2 shocks which suffer only rather little extinction, as they have HH-object counterparts at optical wavelengths.

The L1641 dark cloud belongs to opacity class 4 in the scheme of Lynds (1962), where the opacity class corresponds roughly to the optical extinction. However, our H_2 survey is targeted towards the densest parts of L 1641 and the even denser integral-shaped filament in the northern part of Orion A (Bally et al. 1987), and thus the extinction will on average be larger than 4 mag. On one hand, the jets are not all located behind the cloud, but at arbitrary depths within the cloud, thus generally not suffering the full amount of extinction. On the other, the jet driving sources, and therefore parts of the jets, are embedded in the densest molecular clumps leading to a systematically higher than average extinction. Thus, in lieu of any real extinction estimates, we simply assume a K-band extinction of $A_K \sim 1$ mag towards the Orion A H_2 flows, equivalent to $A_V \sim 10$ mag.

As in the case of the jet length, analyses in our subsequent papers of the measured H_2 luminosities of the jets will rely at first on the interpretation of general trends rather than of the actual value of the jet H_2 luminosities. While one again might hope that the various errors in extinction estimates might cancel out across various groupings of flows, it is important to note that there may be a systematically higher extinction towards the flows from the youngest protostars, which are likely to have more circumstellar material and thus extinction.

Finally, the jet H_2 luminosities will also be used to derive estimates of the kinetic energy input rate of the jets, their mass outflow rates, and the underlying mass accretion rates of the protostellar system. Such estimates are necessarily based on additional assumptions, and the uncertainties introduced by these assumptions very likely dominate the overall error budget, rather than any measurement errors.

6. Summary and future prospects

We have made an unbiased area-covering near-infrared survey over a substantial portion of the Orion A giant molecular cloud in search of protostellar H_2 flows. Following Stanke et al. (2000) which presented some first result from the survey, in this second contribution of a series of papers we have presented the full survey data. We have presented a catalogue of individual H_2 emission line features, which we take to represent shocks in

protostellar outflows. Furthermore, we have identified a list of 76 candidate protostellar jets for which we have derived a number of basic properties, including their position and orientation, their length, and their H_2 brightness. These data form the basis for a statistical investigation of the properties of young protostellar jets.

Subsequent papers will include detailed analyses of the jet sample, in addition to results from our ongoing search for the driving sources of these flows. In these analyses, we will search for evolutionary trends in the jet sample, discuss the orientation of the jets with respect to the large-scale magnetic field in Orion A, estimate the mechanical feedback of the jet/protostar population on a star-forming cloud, and discuss its possible implication for cloud stabilisation and self-regulation of star formation.

Acknowledgements. This research would have been impossible without the great support of the Calar Alto observatory staff. We thank Ken'ichi Tatematsu for providing a fits-file of his Orion A CS data. This research has made use of CDS's Astronomical Database SIMBAD and NASA's Astrophysics Data System Abstract Service. We acknowledge the use of NASA's *SkyView* facility (`http://skyview.gsfc.nasa.gov`) located at NASA Goddard Space Flight Center. This work was supported by the *Deutsche Forschungsgemeinschaft, DFG* project number Zi 242/9-1 and Zi 242/9-2.

References

Aspin, C., & Reipurth, B. 2000, MNRAS, 311, 522
Bally, J., & Devine, D. 1994, ApJ, 428, L65
Bally, J., Langer, W. D., Stark, A. A., & Wilson, R. W. 1987, ApJ, 312, L45
Bizenberger, P., McCaughrean, M. J., Birk, C., Thompson, D., & Storz, C. 1998, Proc. SPIE, 3354, 825
Black, J. H., & Dalgarno, A. 1976, ApJ, 203, 132
Bohigas, J., Torrelles, J. M., Echevarría, J., et al. 1985, Rev. Mex. A&A, 11, 149
Bontemps, S., André, P., Terebey, S., & Cabrit, S. 1996a, A&A, 311, 858
Bontemps, S., Ward-Thompson, D., & André, P. 1996b, A&A, 314, 477
Casali, M. M. 1992, JCMT UKIRT Newslett., 4, 33
Chen, H., Tokunaga, A. T., Strom, K. M., & Hodapp, K.-W. 1993, ApJ, 407, 639
Chini, R., Reipurth, B., Ward-Thompson, D., et al. 1997, ApJ, 474, L135 (CRW)
Corcoran, D., & Ray, T. P. 1995, A&A, 301, 729
Davis, C. J., & Eislöffel, J. 1995, A&A, 300, 851
Davis, C. J., Eislöffel, J., & Ray, T. P. 1994, ApJ, 426, L93
Davis, C. J., Dent, W. R. F., Matthews, H. E., Coulson, I. M., & McCaughrean, M. J. 2000, MNRAS, 318, 952
Devine, D., Bally, J., Reipurth, B., & Heathcote, S. 1997, AJ, 114, 2095
Eislöffel, J., & Mundt, R. 1997, AJ, 114, 280
Eislöffel, J., Mundt, R., Ray, T. P., & Rodriguez, L. F. 2000, in Protostars and Planets IV, ed. V. Mannings, A. P. Boss, & S. S. Russell (Tucson, University of Arizona Press), 815
Fukui, Y., Iwata, T., Mizuno, A., Bally, J., & Lane, A. P. 1993, in Protostars and Planets III, ed. E. H. Levy, & J. I. Lunine (Tucson: University of Arizona Press), 603
Gredel, R., & Reipurth, B. 1993, ApJ, 407, L29
Levreault, R. M. 1988, ApJS, 67, 283
Lynds, B. T. 1962, ApJS, 7, 1
Mader, S. L., Zealey, W. J., Parker, Q. A., & Masheder, M. R. W. 1999, MNRAS, 310, 331
McCaughrean, M. J. 1988, Ph.D. Thesis (Edinburgh University)
McCaughrean, M. J., Rayner, J. T., & Zinnecker, H. 1994, ApJ, 436, L189
Morgan, J. A., Schloerb, P. F., Snell, R. L., & Bally, J. 1991, ApJ, 376, 618
Pravdo, S. H., Rodriguez, L. F., Curiel, S., et al. 1985, ApJ, 293, L35
Reipurth, B., & Bertout, C. (eds.) 1997, Herbig-Haro Flows and the Birth of Low Mass Stars, Proc. IAU, 182
Reipurth, B., Heathcote, S., Roth, M., Noriega-Crespo, A., & Raga, A. C. 1993, ApJ, 408, L49
Reipurth, B., Bally, J., & Devine, D. 1997, AJ, 114, 2708
Reipurth, B., Devine, D., & Bally, J. 1998, AJ, 116, 1396
Richer, J., Shepherd, D., Cabrit, S., Bachiller, R., & Churchwell, E. 2000, in Protostars and Planets IV, ed. V. Mannings, A. Boss, & S. Russel (Tucson: University of Arizona Press), 867
Shull, J. M., & Hollenbach, D. J. 1978, ApJ, 220, 525
Smith, M. D. 1995, A&A, 296, 789
Stanke, T. 2000, Ph.D. Thesis, Universität Potsdam
Stanke, T., McCaughrean, M. J., & Zinnecker, H. 1998, A&A, 332, 307
Stanke, T., McCaughrean, M. J., & Zinnecker, H. 2000, A&A, 355, 639
Strom, K. M., Strom, S. E., Wenz, M., Wolff, S. C., & Morgan, J. 1986, ApJS, 62, 39
Strom, S. E., Strom, K. M., Grasdalen, G. L., et al. 1985, AJ, 90, 2281
Tatematsu, K., Umemoto, T., Kameya, O., et al. 1993, ApJ, 404, 643 (T93)
Yu, K. C., Bally, J., & Devine, D. 1997, ApJ, 485, L45
Zinnecker, H., McCaughrean, M. J., & Rayner, J. T. 1998, Nature, 394, 862